AN ABSTRACT OF THE THESIS OF

Alejandro Lopez for the degree of Master of Science in Radiation Health Physics presented on April 27, 2006.
Title: Determination of Phoswich Detector Response Using MCNP Analysis to Enhance Radioxenon Measurement.

Abstract approved:

Redacted for Privacy

David M. Hamby

As mandated by the Comprehensive Nuclear Test Ban Treaty (CTBT), the United States (US) is involved in the development and deployment of an International Monitoring System (IMS) for monitoring nuclear explosions. The US system, developed at Pacific Northwest National Laboratory, is known as the Automated Radioxenon Sampler/Analyzer (ARSA). The US plans to implement a large number of monitoring stations around the world, so reductions must be made in power requirements, complexity, size and cost. Research suggests the potential of using a Phoswich-based detector system that will meet these reduction requirements while increasing reliability of nuclear-detonation radioxenon detection. In 2005 the research team at Oregon State University began seeking ways to optimize detection of radioxenon gas produced during fission processes, including the detonation of nuclear weapons. The research described herein is part of this effort.

The objectives of this research are as follows: (1) to review fission mechanisms for radioxenon production, (2) to model a triple-layer prototype phoswich detector and determine detector response on exposure to radioxenons, and (3) to predict detector responses from various energy deposition patterns. Monte Carlo N-Particle (MCNP) version 5 was used to model the phoswich detector and to simulate energy deposition from radioxenon sources.

The simulations revealed that the phoswich detection system achieves excellent detection of photon and electron energies associated with radioxenon decay. Probabilities of radioxenon photon interactions in the three scintillation crystals were determined. By tracking the history of a photon, the simulation data was correlated into pulse shapes. The pulses were analyzed by a component analysis (CA) algorithm yielding accurate pulse component discrimination.

Determination of Phoswich Detector Response Using MCNP Analysis to Enhance Radioxenon Measurement

by

Alejandro Lopez

A THESIS

submitted to

Oregon State University

in partial fulfillment of
the requirements for the
degree of

Master of Science

Presented April 27, 2006
Commencement June 2006

Master of Science thesis of Alejandro Lopez presented on April 27, 2006.

APPROVED:

Redacted for Privacy

Major Professor, representing Radiation Health Physics

Redacted for Privacy

Head of the Department of Nuclear Engineering and Radiation Health Physics

Redacted for Privacy

Dean of the Graduate School

I understand that my thesis will become part of the permanent collection of Oregon State University libraries. My signature below authorizes release of my thesis to any reader upon request.

Redacted for Privacy

Alejandro Lopez, Author

TABLE OF CONTENTS

TABLE OF CONTENTS (Continued)

Page

LIST OF FIGURES

LIST OF FIGURES (Continued)

Figure Page

LIST OF TABLES

DETERMINATION OF PHOSWICH DETECTOR RESPONSE USING MCNP ANALYSIS TO ENHANCE RADIOXENON MEASUREMENT

Chapter 1 INTRODUCTION

As mandated by the Comprehensive Nuclear Test Ban Treaty (CTBT), the United States (US) government is involved in the development and deployment of an International Monitoring System (IMS) for monitoring nuclear explosions. Four radiation monitoring systems have been developed around the world, all based on the detection of radioxenons released during a nuclear detonation. The US system, developed at Pacific Northwest National Laboratory, is known as the Automated Radioxenon Sampler/Analyzer (ARSA). The US plans to implement a large number of monitoring stations around the world. Oregon State University (OSU) has been conducting research on radiation detection in mixed beta/gamma radiation fields for the past seven years (Bush-Goddard 2000, Kriss and Hamby 2003; 2004a; 2004b; 2004c; Tavakoli-Farsoni and Hamby 2004a; 2004b). Research suggests that the OSU phoswich-based detector system is appropriate to reduce power requirements, complexity, size, and cost of the current ARSA system. In 2005, the research team at OSU began seeking ways to optimize detection of radioxenon gasses produced during the fission process, including the detonation of nuclear weapons. The research described herein is part of this effort.

The objectives of this research are as follows: (1) to review fission mechanisms for radioxenon production, (2) to model a prototype phoswich detector

for determination of detector response on exposure to radioxenons, and (3) to predict detector response from various energy deposition patterns.

Fission mechanisms are reviewed by examining Q-values, energy balance, fission product yield, and by determining the fission yield of two historical explosions, namely those at Hiroshima and Nagasaki in 1945. Particular attention is given to radioxenon gasses, specifically ^{131m}Xe, ^{133}Xe, ^{133m}Xe, and ^{135}Xe, produced during high energy fission.

A 3rd generation triple-layer phoswich detector is modeled using the Monte Carlo N-Particle (MCNP) transport code. The exposure source consists of specific combinations of ^{131m}Xe, ^{133}Xe, ^{133m}Xe, and ^{135}Xe dependent on time after fission of uranium-235 (^{235}U) and plutonium-239 (^{239}Pu). Utilizing a first order kinetic model, the amount of each xenon isotope is determined from the instant of detonation through each fission decay chain until detection is no longer feasible.

Once the detector has been successfully modeled and energy deposition in each layer from both photons and electrons has been determined, the data will be used to generate detector response and expected output (i.e. pulse shape). Pulse shape simulation will allow validation of a component analysis algorithm (developed at OSU) to determine the feasibility of extracting energy deposition information, as a function of scintillation layer, from each phoswich signal pulse.

Chapter 2 BACKGROUND

2.1 Nuclear Explosion Monitoring

In 1996, the United States (US) was the first country to sign the Comprehensive Test Ban Treaty (CTBT) as an international effort to ban all nuclear weapons test explosions. Since 1996, 160 countries have signed the treaty. The CTBT requires the development and deployment of an International Monitoring System (IMS) for monitoring nuclear explosions. Monitoring may be achieved through seismic, infrasound, hydroacoustic, and radionuclide measurements (US State Department 2001). The radionuclide monitoring system developed in the US by Pacific Northwest National Laboratory is known as the Automated Radioxenon Sampler/Analyzer (ARSA). Detection is achieved with two large sodium iodide (NaI(Tl)) crystals and four plastic scintillators. Each of these detectors requires its own pair of photomultiplier tubes (PMTs) and independent electronic circuits. These twelve PMTs create a large amount of complexity, particularly with gain matching and calibration, not to mention their large size, high power consumption, and high cost to manufacture.

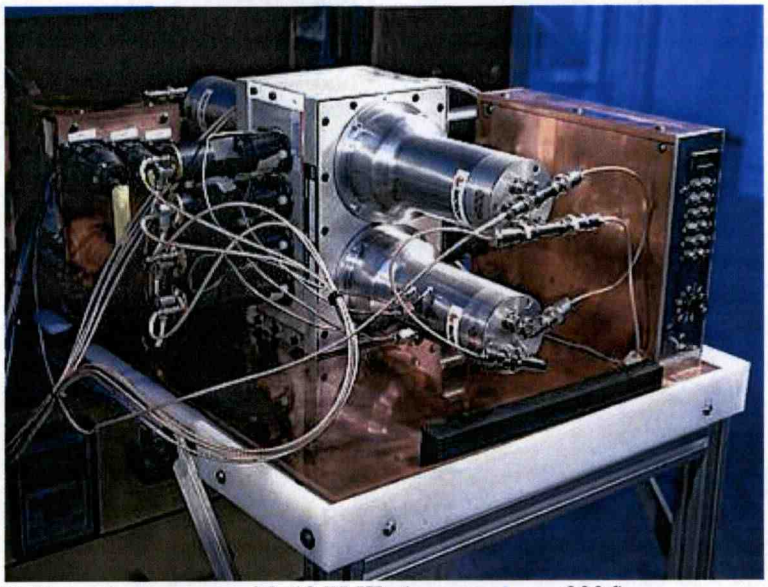

Figure 2.1 ARSA Detection system with 12 PMTs (www.pnl.gov 2006).

As the US plans to implement a large number of monitoring stations around the world, reductions in power requirements, complexity, and size of the current ARSA system are necessary. Ely et al. (2003) explored the idea of using a phoswich detector for the ARSA consisting of a calcium fluoride ($CaF_2(Eu)$) scintillator coupled to a NaI(Tl) crystal. This system only requires a total of one PMT per phoswich, thus greatly reducing power requirements and complexity. Utilizing a digital pulse processor, signals from each scintillator can be distinguished and separated to determine beta vs. gamma contributions. The phoswich detection system developed at OSU utilizes multiple scintillators, pulse component analysis, and high-speed digital signal processing to better characterize and separate beta and gamma energy deposition spectra.

2.2 Fission

Nuclear fission occurs when the nucleus of an atom splits into two or more nuclei as fission products. Fission is induced when a fissionable atom absorbs a neutron, increasing the excitation energy and deforming the nucleus. If ^{235}U is the fissionable atom, about fifteen percent of these excited nuclei (^{235}U+ neutron) decay by gamma emission, while the other eighty-five percent undergo fission and break apart into two large fragments and several neutrons (Martin 2004). The liberated neutrons are then able to induce fission of additional nuclei, resulting in a potential chain reaction. Nuclear weapons are based on the process of an uncontrolled fission chain reaction.

The nuclides ideal for a nuclear weapon are those with a high probability of fission reaction, that yield a high number of excess neutrons, that have a low probability of absorbing neutrons without a fission reaction, and that have a low spontaneous fission rate. The primary nuclides which fit these criteria are ^{235}U, ^{239}Pu, and ^{233}U (Glasstone and Dolan 1977). Uranium-235 and ^{239}Pu are the fissile materials most often used in atomic bombs and will be the focus of this research[1].

In order for a successful fission to occur, the nucleus must separate by overcoming the activation energy or energy barrier. The amount of energy required to overcome the energy barrier is 5.2 million electron volts (MeV) for ^{235}U and 4.8 MeV for ^{239}Pu (Martin 2004). Directly after the nucleus separates, the two positively

[1] Several ^{233}U bombs have been detonated by the US, and it may be a component of India's weapons program. Other isotopes have been considered as potentially useable in fission weapons, though no country has been known to produce them for this purpose (www.wikipedia.org 2006)

charged fission fragments receive a total of about 165 MeV of kinetic energy from their Coulomb repulsion. Neutrons, as well as prompt gamma-rays emitted at the instant of fission, receive about 12 MeV of emitted energy[2]. The remainder of the energy (approximately 25 MeV) is released through decay of the fission products over time (Glasstone and Dolan 1977). The total amount of energy liberated per fission is about 200 MeV. One example of a fission reaction is shown below, where Q is the energy released in the reaction.

$$^{235}U + {}^{1}_{0}n \rightarrow {}^{236}U^{*} \rightarrow {}^{147}Sm + {}^{87}Rb + 7\,{}^{0}_{-1}\beta^{-} + 2\,{}^{1}_{0}n + Q$$

$$Q = 193.139 MeV$$

As stated earlier, multiple fission products can be produced during a single fissioning event. The atomic numbers (Z) of the fission fragments range from 30 to 64 from the fission of ^{235}U or ^{239}Pu (Cember 1996). Most fission fragments are radioactive due to the fact that they were produced from a nucleus containing a neutron to proton ratio of about 1.5, while stable nuclides with a Z of 30 to 64 have much lower ratios of around 1.3 (Lilley 2004). The neutron rich fragments decay by way of beta-particle emission, gamma emission, and occasionally neutron emission until stability is achieved. This sequence of decay is known as the fission decay chain. The decay chain for an atomic mass number of 133 is shown in Figure 2.2. All nuclides in the chain are created as a result of fission, with all of these eventually decaying to ^{133}Cs.

---

[2] The fission of uranium or plutonium can result in multiple fission products including the release of an average of 2.44 neutrons and several gammas (Martin 2004)

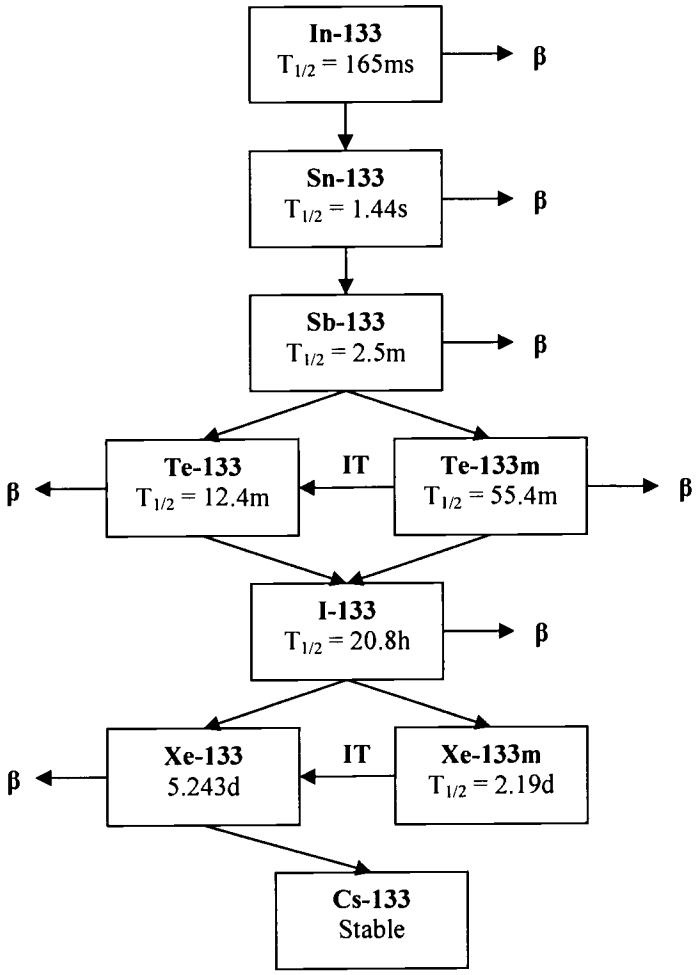

Figure 2.2 Sample Fission Decay Chain.

2.2.1 Hiroshima and Nagasaki

In 1964, the 3rd edition of *The Effects of Nuclear Weapons* was released by Samuel Glasstone and Philip J. Dolan. This book was prepared and published by the US Department of Defense and the Energy Research and Development Administration. Topics of interest covered in the book include general principles of nuclear explosions, descriptions of underground bursts, and characteristics of both shallow and deep underground bursts.

The Effects of Nuclear Weapons published information regarding the basic fission principles involved in a high energy explosion, including the following data:

1 KILOTON OF TNT[3] = **• Complete fission of 0.057 kg (57 grams or 2 ounces) fissionable material**
• Fission of 1.45×10^{23} nuclei
• 2.6×10^{25} MeV

For the purpose of this paper, a "typical" weapons test is assumed to be either the ^{235}U bomb (Little Boy) dropped over Hiroshima on August 6th, 1945, or the ^{239}Pu bomb (Fat Man) dropped on Nagasaki on August 9th, 1945. Estimations of fission yield of Little Boy vary from source to source, but according to Glasstone and Dolan, approximately 2 pounds of uranium fissioned in the explosion. This is roughly equivalent to 15,000-16,000 tons of TNT. The approximate number of fissions during this explosion is calculated as follows:

$$1 kiloton = 1.45x10^{23} \frac{nuclei}{kiloton}$$

$$\left(1.45x10^{23} \frac{nuclei}{kiloton}\right)(15.5 kilotons) = 2.2x10^{24}\ fissions$$

Again, according to Glasstone and Dolan, 2 pounds of plutonium fissioned in the Fat Man explosion (about 22 kiloton yield) resulting in approximately $3.2x10^{24}$ fissions. This is roughly equivalent to a total energy release of about 6.4×10^{26} MeV for the plutonium explosion and about 4.5×10^{26} MeV for the uranium explosion.

[3] Typical yield of an atomic explosion is equated to the amount of energy released in an explosion of tri-nitrotoluene (TNT).

2.3 Radioxenon

Both surface and subsurface nuclear explosion monitoring are of great concern. Subsurface monitoring presents much more unique and difficult challenges for explosion detection. The explosion of a nuclear weapon under the ground will produce a sphere of high pressure and high temperature gas, similar to the fireball in a surface detonation. As expected, if the nuclear explosion occurs deep enough beneath the surface of the earth, many fewer fission products will be released into the atmosphere (Glasstone and Dolan 1977). The detection of underground nuclear explosions can be achieved or confirmed through the measurement of released fission products.

Several fission products were initially chosen as possible nuclides of interest because they have half-lives of several hours to several years, high specific activity, and relatively large fission yields. Certain fission products, namely the noble gasses, can "be expected to percolate through porous earth and escape the cavity of an underground nuclear explosion" (Robbins et al. 2002). The four noble gas fission products of particular interest for nuclear explosion monitoring purposes are ^{131m}Xe, ^{133m}Xe, ^{133}Xe, and ^{135}Xe. These four radioxenons have half-lives of 11.9 days, 2.19 days, 5.24 days, and 9.10 hours, respectively.

The four xenon isotopes of primary concern have distinctive decay properties allowing them to be distinguished from other radionuclides whether natural background, radon decay progeny, or man-made sources. Xenon-131m decays to ^{131}Xe by emission of a 164 kilo electron volt (keV) gamma (2% of the time) or by a

129 keV conversion electron decay (61% of the time) typically accompanied by a 30 keV X-ray (54% of the time). The decay of ^{133m}Xe occurs by emission of a 233 keV gamma (10% yield), or while releasing a 199 keV conversion electron (64% yield) and a corresponding x-ray at 30 keV (56% yield). Using the conversion electron and subsequent x-ray, a unique signature is produced in a beta-gamma coincidence counting system to identify each of these nuclides. The remaining two nuclides decay primarily by beta decay. Xenon-133 decays with a maximum beta energy of 347 keV accompanied by emission of an 81 keV gamma with a 38% yield. A conversion electron is also emitted (61% yield) with an energy of 129 keV. Xenon-135 decays by emitting a beta particle with a maximum energy of 905 keV, and also has a 250 keV gamma (90% yield). Similarly, a conversion electron is emitted with ^{135}Xe (6% yield) with an energy of 214 keV. Table 2.1 summarizes the decay properties of each xenon isotope of interest.

Table 2.1 Dominant Decay Modes of the Radioxenon Isotopes

Nuclide	^{131m}Xe	^{133m}Xe	^{133}Xe	^{135}Xe
X-rays				
Energy (keV)	30	30	31	31
Yield (%)	54	56	49	5
Gamma-rays				
Energy (keV)	164	233	81	250
Yield (%)	2	10	38	90
Conversion Electrons				
Energy (keV)	129	199	45	214
Yield (%)	61	64	55	6
Beta				
Max. Energy (keV)	-	-	347	905
Yield (%)	-	-	99	97

2.3.1 Radioxenon Concentration Ratios

There are several sources of radioxenon around the world, including nuclear reactors, medical procedures, nuclear fuel reprocessing, and nuclear weapons testing. The expected concentration ratios of radioxenons vary depending on the nuclear process. One important paper, with substantial detail on ratio analysis, was completed by Heimbigner et al. (2002) at Pacific Northwest National Laboratory (PNNL). The publication presents results of ARSA measurements taken at several locations around the world including; Richland, WA; New York City, NY; Charlottesville, VA; Freiburg, Germany; and Guangzhou, China.

Measurements at these locations identified various concentration ratios of radioxenon gasses. The ratios were then attributed to nuclear fission sources including medical facilities, nuclear reactors, and fuel reprocessing plants. Particularly important to this research was a figure displaying expected activity ratios for ^{131m}Xe:^{133}Xe, ^{133m}Xe:^{133}Xe and ^{135}Xe:^{133}Xe with respect to time after a subsurface nuclear detonation. The figure also displayed the same three radioxenon ratios expected from an operating reactor to demonstrate the reactor ratios are all lower than nuclear detonation ratios. Figure 2.3 shows the expected ratios from the fission of ^{235}U re-created from Heimbigner et al. (2002).

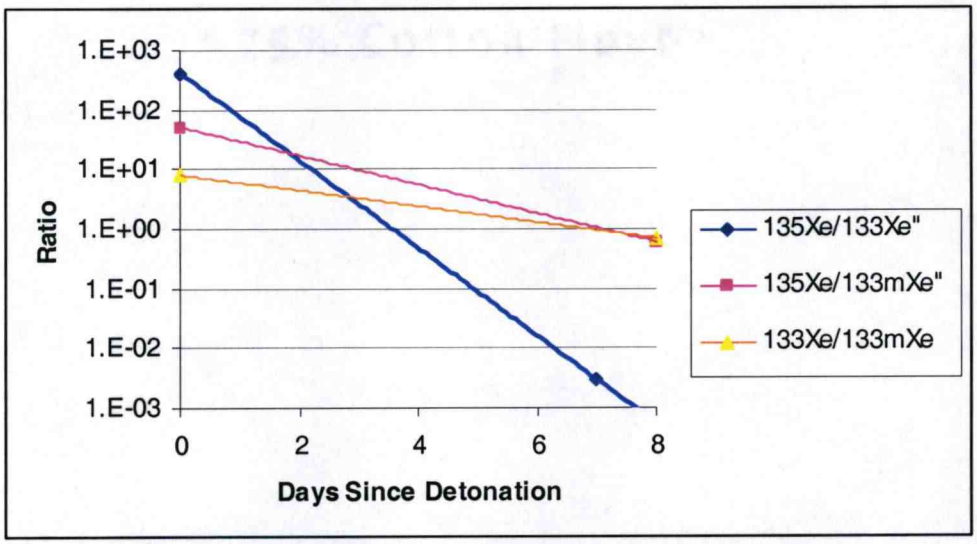

Figure 2.3 Expected activity ratios for 133Xe/133mXe, 133Xe/133mXe and 135Xe/133Xe from a subsurface nuclear detonation recreated from Heimbigner et al. 2002.

2.4 Scintillation Detectors

Scintillation detectors are based on the collection of scintillation light produced in certain materials when interacted upon by ionizing radiation. An ideal scintillator will possess the following characteristics: high detection efficiency, linear light output, good optical quality, and a short decay time (Knoll 2000). Scintillation detectors have been shown to be excellent beta and gamma detectors, depending on the material type, thickness, and shape. There are two basic types of scintillators: organic and inorganic.

Organic scintillators are typically of low Z and low density, and have a short light decay time constant. An organic detector functions by excitation of an entire molecule, and emits visible light during de-excitation. Molecular excitation is therefore independent of the physical state of the detector. Types of organic detectors include pure organics, liquids, plastics, films, loaded organics, and gases (Knoll 2000).

Inorganic scintillators are based on light emission from the crystal lattice of the material through excitation and de-excitation. If sufficient incoming energy is absorbed, an electron can elevate from its normal lattice position, leaving a vacancy. As the electron returns to fill the vacancy, a photon (visible light) is emitted. The visible light (emitted in both an inorganic and organic scintillator) will be detected by a photomultiplier. The photons will produce photoelectrons from the photocathode surface of the photomultiplier. These electrons are multiplied through a series of dynodes until a final avalanche of electrons arrives at the anode and produces an electrical pulse. This pulse is proportional to the energy initially deposited in the crystal (Knoll 2000).

2.5 Photon Interactions

The detection of gamma-rays or x-rays through scintillation is based on photon interaction via three primary mechanisms: photoelectric absorption, Compton scatter, and pair production. In a NaI(Tl) crystal, photoelectric absorption predominates at low energies (0~250 keV), Compton scatter is the most probable interaction for energies between 250 keV and 5 MeV, and pair production predominates at higher energies (5-10 MeV) (Martin 2004).

During photoelectric absorption, an incoming photon will interact with and eject a tightly bound inner-shell electron. The electron will possess kinetic energy equal to the photon energy minus the binding energy of the orbital from which it was ejected. The vacancy is promptly filled, causing the emission of characteristic iodine

x-rays, which are most likely immediately absorbed by the crystal. The resulting signal will produce a full-energy photopeak if all of these interactions occur relatively quickly. Photoelectric absorption probabilities vary strongly with the energy of the incoming photon and the Z of the material.

Photon energies greater than about 250 keV and less than 5 MeV will most likely undergo Compton interactions. An incoming photon is deflected through an angle, θ, with respect to its original direction, by a lightly bound or free electron in the absorbing material. A portion of the energy of the photon is transferred to the electron. The greater the angle of deflection (up to 180°), the greater the energy transferred to the electron. Unlike the photoelectric effect, the probability of Compton scatter is less dependent on the incident photon energy and the Z of the absorbing material, but directly dependent on the density of electrons in the medium.

For higher energy photons, pair production predominates. A minimum energy of 1.022 MeV is necessary for pair production to occur as the entire photon energy is converted into the creation of an electron-positron pair (2 rest masses of 0.511 MeV each). Since the maximum incoming photon energy associated with the four radioxenon isotopes is 250 keV, pair production will not be possible and photoelectric interactions are most likely, assuming other sources can be discriminated.

2.6 Beta Interactions

Beta particles (electrons) interact by two primary mechanisms; coulombic interactions and radiative bremsstrahlung interactions. During coulombic events, an electron may exchange nearly all of its energy in a single "collision" by dislodging an orbital electron in the absorbing material to create ion pairs. The energy carried by these excited ion pairs is absorbed at the interaction site. Electrons can be ejected from the K-, L-, or M-shells and are accompanied by the emission of characteristic x-rays. Bremsstrahlung radiation is the result of charged particle deceleration where an electron is passing through matter and the Coulombic interactions cause sudden changes in velocity. As an electron passes near a nucleus, it experiences deceleration due to the deflecting force and loses energy as bremsstrahlung photons. The amount of energy lost via bremsstrahlung depends on the atomic number of the absorbing nucleus and the energy of the electron. Bremsstrahlung production is greatest with high-energy electrons decelerating in high Z materials.

2.7 Phoswich Detector

The combination of two or more different scintillators "sandwiched" together and coupled to a single PMT creates a phoswich detector. Each scintillator has a characteristic light decay time resulting in a unique signal pulse. The electronic signals produced in a phoswich can be distinguished from each other by differentiating fast and slow signal components, allowing the determination of which scintillator the interaction occurred in. The most common combination of scintillation materials

chosen for typical phoswich detectors is sodium iodide coupled with cesium iodide because their decay times are quite different, allowing their corresponding pulses to be easily distinguished (Knoll 2000).

By using a thin layer scintillator, shallow penetrating radiation can be fully stopped in the first layer, while more penetrating particles can interact in both layers. Utilizing these particle discriminating capabilities, phoswich detectors have been used as beta-gamma dosimeters (Kriss and Hamby 2004a), gamma telescopes (Grindlay et. al 1994), and heavy ion detectors (Pak et. al 1996). Typically, only two layers are used in a phoswich detector.

It was suggested by Ely et al. (2003) that improvements to the current ARSA system could be made based on detection by analysis of signals from a phoswich detector. Approaches taken by Ely et al. (2003) did not allow for detection of coincidence events nor sufficient precision of beta and gamma energy measurements for radioxenon monitoring. The research presented by Hennig et al. (2004) made a strong case for the implementation of phoswich detectors into the ARSA system. Using a beta and gamma detector optically coupled would greatly simplify coincidence measurement with minimal performance loss.

The objective of Hennig et al. (2004) was to improve known methods of coincidence detection with a phoswich detector for eventual implementation into the ARSA system. Experimentation was performed using a plastic scintillator known as BC-404 optically coupled to a CsI(Tl) crystal. A prototype design was also modeled in MCNP with improved geometry to increase xenon measurement efficiency with the

objective of optimizing phoswich layer thicknesses. An algorithm was successfully developed that allowed the authors to achieve clear separation of beta only, gamma only, and coincidence events, as well as accurate measurements of both beta and gamma energies. A triple-layer detector developed at the University of Michigan in the late 90's (Bush-Goddard and Hamby 2000) and further investigation at Oregon State (Tavakoli-Farsoni and Hamby 2004a) extends the capabilities of the detection system to better differentiate beta from gamma radiation.

Chapter 3 MATERIALS AND METHODS

3.1 Ratio Determination

Previous work (Heimbigner 2002) resulted in expected concentration ratios for various radioxenon combinations from several nuclear sources. By examining particular ratios between the four isotopes, ^{131m}Xe, ^{133}Xe, ^{133m}Xe, and ^{135}Xe, the origin of the radioxenon can be identified. Although the methodology was not specified in great detail by Heimbigner (2002), similar ratios following a nuclear explosion were created in this work. The primary ratios of concern are ^{131m}Xe:^{133}Xe, ^{133m}Xe:^{133}Xe, and ^{135}Xe:^{133}Xe. As mentioned earlier, it is evident that the expected activity ratios for ^{133m}Xe:^{133}Xe, and ^{135}Xe:^{133}Xe from a nuclear detonation are higher than those ratios resulting from reactor operations (Heimbigner 2002).

Determining the time-dependent concentration of each xenon isotope required the development of a first order kinetic model that simulates each of the appropriate xenon decay chains. Models were designed with the STELLA[4] software package. STELLA allows the user to create complex numerical models with the aid of a graphical interface. As the model is constructed, the software automatically creates an algorithm with user-defined input data to generate a solution to the numerical model. Outputs can be observed numerically or graphically. The graphical representation of the ^{131m}Xe decay chain created in STELLA is provided in Figure 3.1.

[4] STELLA is a software package created by isee systems inc., Wheelock Office Park 31, Old Etna Road, Suite 5N, Lebanon, NH 03766 USA.

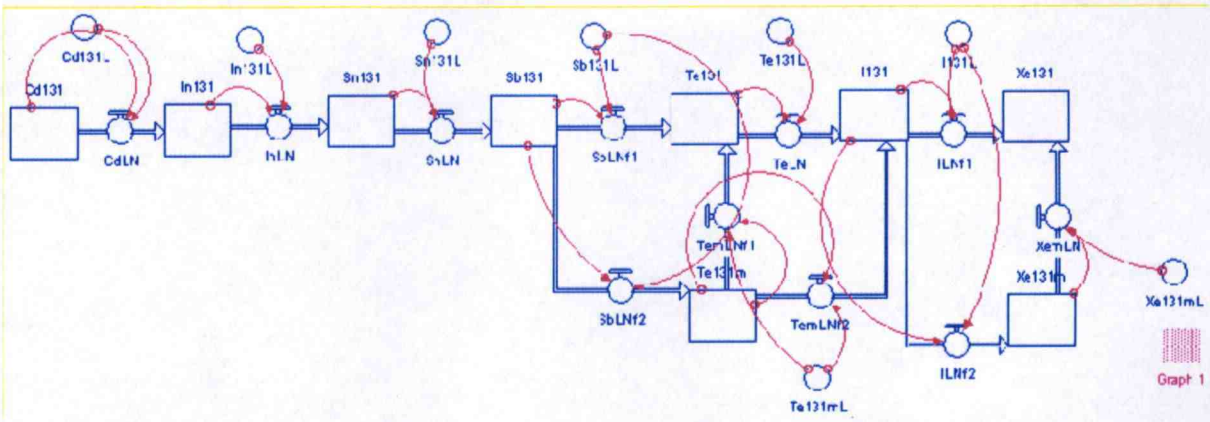

Figure 3.1 ^{131}Xe (ENDF[5]) Decay Chain created in STELLA beginning with ^{131}Cd on the left and ending with stable ^{131}Xe on top right.

Initial fission yields of each nuclide in the chain created from high energy fission of both ^{235}U and ^{239}Pu, were entered into separate models relating to the four specific radioxenons of interest. Initial fractions (in percentage of fissions) of nuclides created along the ^{131}Xe decay chain from high-energy fission of ^{235}U are given in Table 3.1. ENDF fractions used in STELLA models for the other three xenon chains can be found in Appendix A.

Table 3.1 ENDF Fraction of radionuclides produced from high-energy fission of ^{235}U

Nuclide	Fission Yield (%)
Cd-131	1.38E-05
In-131	0.007163
Sn-131	0.368568
Sb-131	2.150054
Te-131m	1.164511
Te-131	0.29159
I-131	0.120171
Xe-131m	0.000909
Xe-131	0.000199

[5] ENDF is a nuclear reaction database containing information including evaluated cross sections, angular distributions and fission product yields. ENDF database is stored at National Nuclear Data Center, Brookhaven National Laboratory and Los Alamos National Laboratory.

Fission yields were also entered into the ^{133}Xe and ^{135}Xe decay chain models. The model was compartmentalized and decay constants were included for all decay paths. The STELLA model then solves the set of differential equations generated by the user through the graphical interface. The number of atoms of each nuclide in the decay chain can then be determined as a function of time. All models were run with fission yield data for both ^{235}U and ^{239}Pu to simulate high-energy fission during a nuclear explosion.

3.2 Triple Layer Phoswich Detector

As noted earlier, researchers at OSU are in the process of developing a multi-layer phoswich detector optimized for radioxenon gas. The current 3rd generation phoswich system consists of three different scintillation materials sandwiched together, each with a unique light decay time allowing for differentiation between beta and gamma energy-deposition events. The detector was manufactured by BICRON[6] in 2005. The first two layers are for beta detection while the third layer is primarily for gamma detection (see Figure 3.2). All materials are housed in an aluminum casing and are coupled to a single PMT.

[6] Bicron designs and manufactures products for radiation detection, measurement, and imaging, along with crystal optics and scintillators (www.bicron.com 2006)

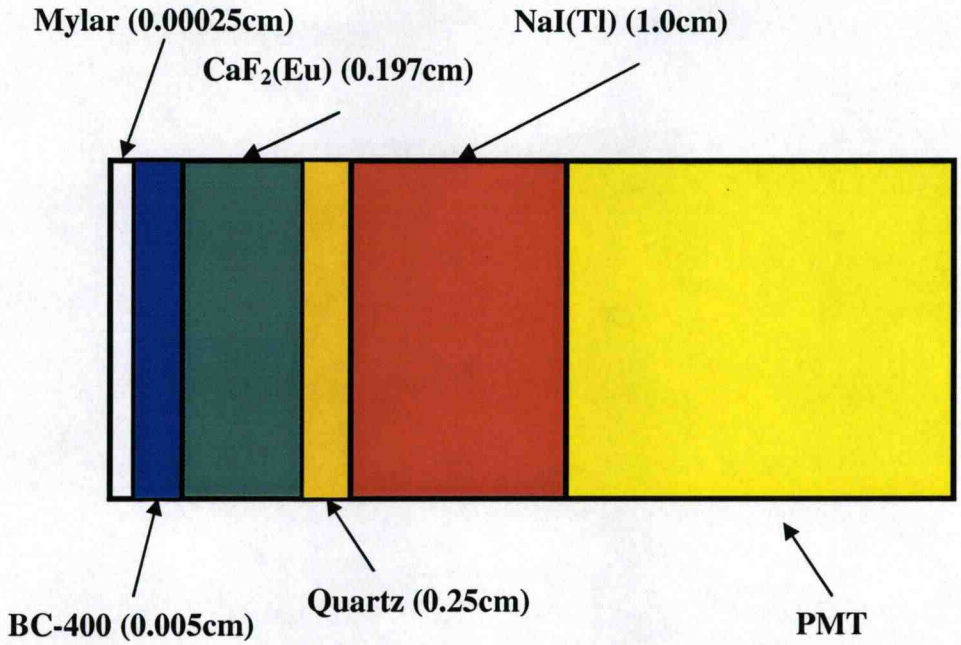

Figure 3.2 Side view of triple-layer phoswich detector with respective thicknesses.

3.2.1 BC-400

The first scintillation layer (closest to the source) of the triple layer sandwich is a plastic scintillator with the trade name BC-400. BC-400 is a general purpose organic scintillator made from aromatic hydrocarbons (purely from hydrogen and carbon). Because of the low Z, low density, and low volume (BC-400 layer is only 50 microns thick), its primarily purpose is to scintillate with low energy beta and conversion electrons. The primary decay time of BC-400 is 2.4 ns which is much smaller than the decay times of the other two scintillation layers.

3.2.2 CaF_2(Eu)

Calcium fluoride is the second active layer of the phoswich system with a primary light decay time of 940 ns. It is an inorganic binary scintillator possessing

unique properties allowing for many detector applications. Calcium fluoride is used for detection of gamma rays up to several hundred keV and for the detection of charged particles. Calcium is the bulk scintillator with the addition of fluoride (to improve efficiency) and europium. The third component (Eu), is an impurity added to enhance the probability of visible photon emission during the de-excitation process; it creates an energy state within the forbidden gap through which the electron can de-excite back to the valence band (Knoll-2002). The low atomic number of CaF_2 makes the material ideal for the detection of beta-particles due to a minimal amount of backscatter and low photon interaction cross section. According to the manufacturer, thin layers of CaF_2(Eu) have been used with NaI to make phoswich detectors capable of separating alpha, beta, and gamma radiation. The combined thickness of the CaF_2(Eu) layer and the BC-400 layer in the prototype detector is only 2.02 mm. This thickness is enough to stop beta particles with energies up to about 1.4 MeV. The maximum beta energy expected from the four xenon isotopes is only 905 keV, so for a detector that is truly optimized for radioxenons, a thinner slice of CaF_2(Eu) could be used.

In the protocol to be established for the radioxenon detector, simultaneous interactions in both the BC-400 and CaF_2(Eu) would yield an accepted beta pulse, as a gamma particle will pass through the thin layers because of its low interaction probability. If an incoming particle interacts with only one of the first two layers, the pulse would be rejected, as it is most likely the result of a photon interaction.

3.2.3 NaI(Tl)

The third scintillator (farthest from the source) is sodium iodide, the most common inorganic scintillator. Similar to CaF_2(Eu), a sodium iodide scintillator is a binary product containing two components. Iodine is the bulk scintillator, with sodium added to increase efficiency. A third element, Thallium, is added to enhance detectable photon emissions. Crystals of NaI(Tl) have a decay time of 250 ns, a very high scintillation efficiency, and are available in a variety of sizes and shapes. As stated above, all beta particles with energies less than 1.4 MeV will be stopped in the first two layers, so interactions occurring in the NaI(Tl) are attributed to photons. Table 3.2 summarizes various properties of each of the three scintillators in the third generation phoswich.

Table 3.2 Properties of scintillation materials from data sheets provided by BICRON.

Scintillator	Density (g/cm3)	Primary Decay Time (ns)	Refractive Index	Relative Light Output	Light Output (photons/MeV)
BC-400	1.032	2.4	1.581	0.26	9.88E+03
CaF2(Eu)	3.18	940	1.47	0.50	1.90E+04
NaI(Tl)	3.67	250	1.85	1.0	3.80E+04

3.2.4 Quartz

Between the CaF_2(Eu) scintillator and the NaI(Tl) scintillator is a layer of quartz. Unlike CaF_2(Eu) crystals, NaI(Tl) crystals are hygroscopic and will deteriorate in the presence of water vapor. Plastic scintillators are inherently wet, so quartz is added as part of an hermetic seal around the NaI(Tl). The quartz does not affect light produced in any of the scintillation crystals and is transparent to that light.

Figure 3.3 Third generation phoswich detector housed in aluminum.

3.3 Phoswich Detector Model

3.3.1 MCNP

Monte Carlo analysis is a technique based on the use of random numbers to predict probabilistic events. Individual radiations (photons or particles) are followed along their paths as they interact in user-defined media, thus creating a simulation of energy deposition events. As the number of entities (histories) is increased, the solution becomes more statistically robust. Using a probability distribution function that describes the likelihood of a given event, random sampling is performed to predict the interaction event occurring at a given place in the medium.

This research uses "Monte Carlo-N-Particle" version 5 (MCNP5) software, which is capable of simulating the transport of photons, electrons, and neutrons. The MCNP5 code requires an input deck consisting of three types of cards: surface, cell, and data. The surface card is made up of parameters defining all surfaces necessary to

construct the geometry of the system in which interactions will be modeled. Once all surfaces have been created, cells (or volumes) are developed using the bounding surfaces defined in the surface cards. After all cells have been defined, the user must specify all remaining information in the data cards. Information needed will include source-term data, materials, tally type (see Section 3.3.4), mode, and particle type. MCNP5 software also contains a Visual Editor, a graphical interface that allows the user to setup and visualize the system geometry (see Section 3.3.3).

An MCNP analysis similar to the research presented the current study has been performed elsewhere. The triple crystal phoswich analyzed by Childress and Miller (2002) consisted of a ZnS(Ag) layer for detecting alpha particles, a CaF_2(Eu) scintillator for betas, and a NaI(Tl) scintillator for gamma detection. The simulation used a previous version of MCNP.

Childress and Miller (2002) state that "the use of Monte Carlo computer simulations to estimate interactions in detectors has been shown to yield errors <5% when compared to collected data". This statement strengthens the need for MCNP analysis on the current phoswich system at OSU to obtain vital detector response data. One key conclusion made by Childress and Miller (2002) is that the evaluation of the use of a triple crystal phoswich system instead of three separate detectors must be done to determine the true potential of the phoswich.

3.3.2 MCNP Source Term

The radioactive source for this work was defined as a disk source with a radius of 1.09cm[7] placed directly against the face of the detector. The source emits either photons or beta particles in one direction; directly into the phoswich system. Because no neutron decays occur along the three xenon decay schemes, only photon and electron interactions were simulated in the layers of the phoswich detector. The photon source consisted of all four xenon nuclides (^{131m}Xe, ^{133}Xe, ^{133m}Xe, and ^{135}Xe). Strength and energy was determined using decay schemes (www.nndc.com 2006) and calculated ratios (see Section 3.1). Beta simulations were performed using the beta spectrum of ^{133}Xe. The doping materials (Eu for CaF_2, and Tl for NaI) were not modeled in the MCNP environment as previous phoswich modeling has demonstrated a difference of only 0.2% from non-doped materials (Childress and Miller 2002). One inherent problem with the MCNP code is that only one type of radiation emitted from the source can be modeled at a time, i.e. photons and betas could not be modeled together, thus preventing the simulation of beta/gamma coincidence events.

3.3.3 MCNP Geometry

The MCNP5 input geometry was constructed to model the current phoswich configuration (see Figure 3.2). There are three scintillation crystals, and two other optical layers within the sandwich, all housed in an aluminum casing. The material thicknesses shown in Figure 3.2 were modeled. All materials were defined with a

[7] 1.1cm is the radius of the scintillation crystals, so 1.09 cm was chosen as disc source radius for MCNP simplification.

diameter of 2.2 cm, as specified by the manufacturer. The aluminum casing was 0.05 cm thick with the inside wall immediately against the scintillation crystals. The space beyond the outside wall of the aluminum casing is defined as "void space" as MCNP5 terminates a history once the particle leaves the volume of the detector.

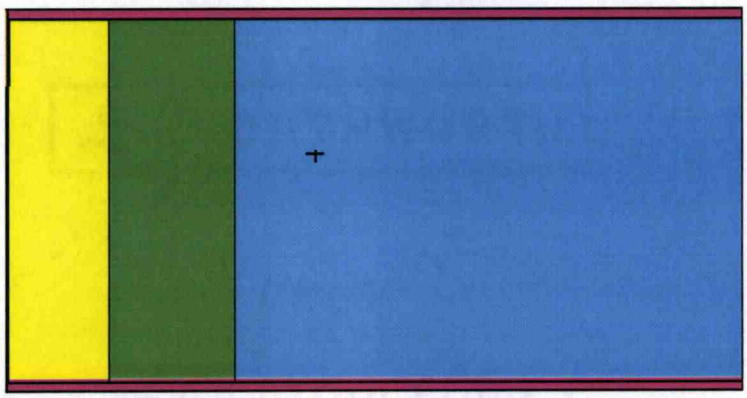

Figure 3.4 Side view of phoswich detector taken from Visual Editor.

Figure 3.4 is a side profile of the detector system. Because the BC-400 layer is so thin (0.005 cm), a magnified figure is shown below taken from the upper left corner of Figure 3.4.

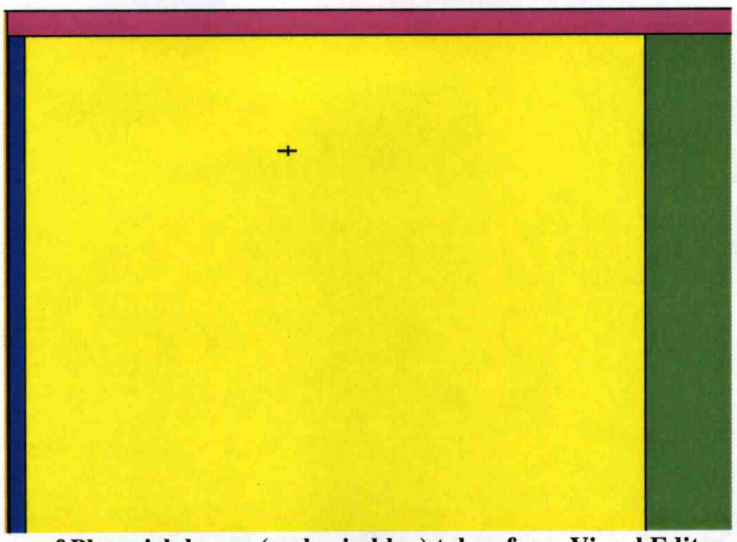

Figure 3.5 Close-up of Phoswich layers (mylar in blue) taken from Visual Editor.

3.3.4 MCNP Tallies

After the photon or electron is emitted from the source and travels into the volume of the detector, a system of MCNP tallies is required in order to determine the amount of energy deposited in each cell. As a history is created for each photon or electron, the information is tallied according to a user-defined tally type. Results of the simulations were reported using a special tally known as an "F8 tally", meaning that pulse height (i.e. energy deposition) was the output parameter of choice. This tally yields probability distributions of energy deposited for a defined set of energy bins. For each scintillation material, a separate F8 tally was applied to model the interactions. Both photon and electron simulations were defined with 2.5 keV-energy bins. Photon simulations were modeled for 20 million source photons while electron simulations modeled 10 million source electrons, yielding relative errors less than 3% in significant energy bins.

3.3.5 MCNP Simulation Description

As mentioned earlier, the simulations were divided into two primary types; those involving photons, and those involving electrons. Photon simulations were run with calculated isotopic ratios at time t=0 hr, 24 hr, and 48 hr after a "typical" weapons test of ^{235}U and ^{239}Pu. Electron simulations were performed using the beta spectrum of ^{133}Xe obtained from Eckerman et al. (1994), as shown below.

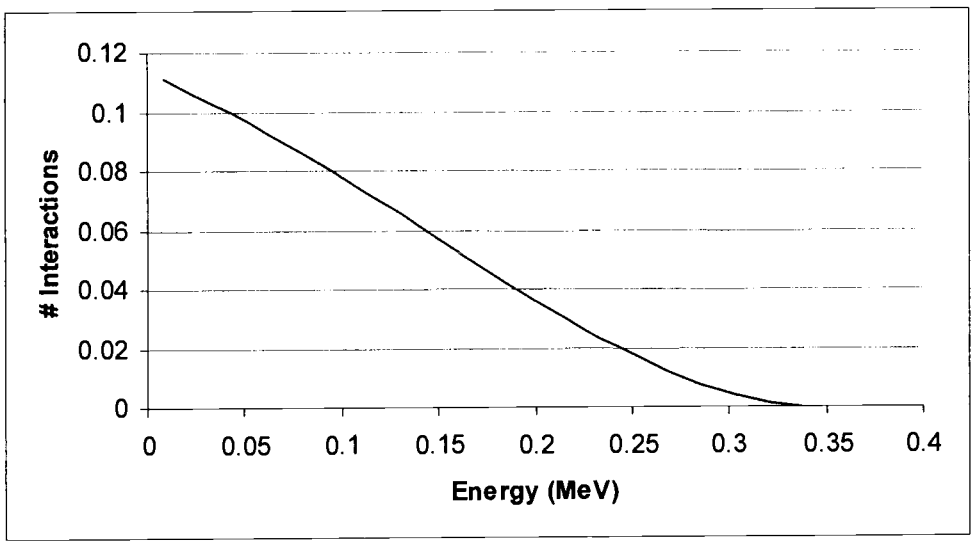

Figure 3.6 Beta Spectrum of ^{133}Xe re-created from Eckerman et al. (1994).

3.4 Determine Detector Response

MCNP is utilized to "acquire" an energy deposition spectrum by simulating the probability of energy deposition events in the phoswich layers. Although this information is important, the true detector response to incoming radiation must be investigated further. The objective here, therefore, is to predict how incoming radiation (photons and electrons) will create unique pulses depending on the specific location of the interactions. There are seven interaction scenarios that are possible in a 3-layer phoswich (see Table 3.3).

Table 3.3 Seven possible combinations of signal light output, with "X" representing the deposition of energy in that particular layer.

Scenario	BC-400	CaF_2(Eu)	NaI(Tl)
1	X		
2		X	
3			X
4	X	X	
5	X		X
6		X	X
7	X	X	X

Incident radiation could theoretically interact in only one layer, in two, or in all three. The likelihood of a beta for example interacting in only the 3rd layer is vanishingly small. The probability of a higher energy photon interacting in the 1st layer is also small. The probability of each of the interaction scenarios is determined in this work for a source of radioxenons.

3.4.1 PTRAC

In order to completely predict detector response (signal pulse shape), the amount of energy deposited, and the layer(s) in which an energy deposition occurs must be determined. This can be achieved using the MCNP parameters described in Section 3.3, with the addition of a card titled Particle Track Output Card otherwise known as PTRAC.

The PTRAC card is a data card in MCNP that allows the user to follow the path of a photon or particle from its creation until termination. The user can specify the amount of information the card will record in an output file produced during a run. PTRAC determines the fate of original photons or particles and can also list the interaction histories of other particles produced from the original particle. This research required PTRAC to record all events[8], the location of all events, and the energy deposition per event. By knowing the event type, location, and energy deposition, the shape of the resultant signal pulse can be determined.

---

[8] PTRAC designates five types of events; (1) a source event, which occurs at the creation of the photon or particle, (2) a bank event which occurs at the creation of a secondary particle, (3) a surface event which occurs when a particle crosses a surface, (4) a collision event, (5) and a termination event which occurs at the end of the particle's history.

Chapter 4 RESULTS AND DISCUSSION

4.1 Concentration Ratio Determination

The concentration of each radioxenon isotope and the resulting concentration ratios for ^{131}Xe:^{133}Xe, ^{133m}Xe:^{133}Xe, and ^{135}Xe:^{133}Xe determined following high-energy fission of ^{235}U are given in Figures 4.1 and 4.2.

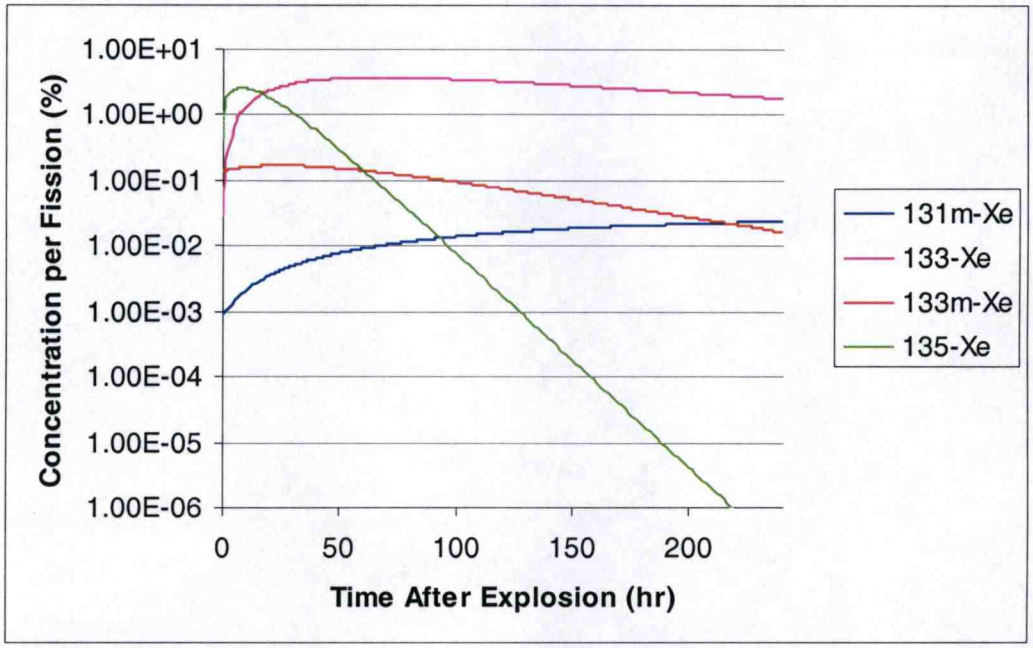

Figure 4.1 Expected Radioxenon concentrations (%) following high-energy fission of ^{235}U.

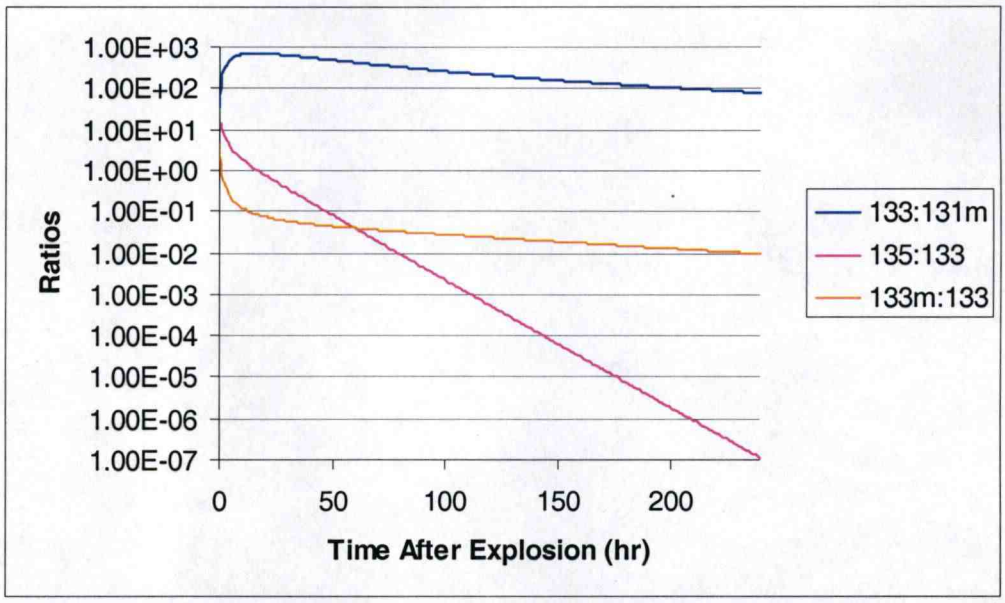

Figure 4.2 Expected radioxenon concentration ratios following high-energy fission of ^{235}U.

Likewise, the concentration of each radioxenon isotope and the resulting concentration ratios for ^{131}Xe:^{133}Xe, ^{133m}Xe:^{133}Xe, and ^{135}Xe:^{133}Xe determined following high-energy fission of ^{239}Pu are given in Figures 4.3 and 4.4.

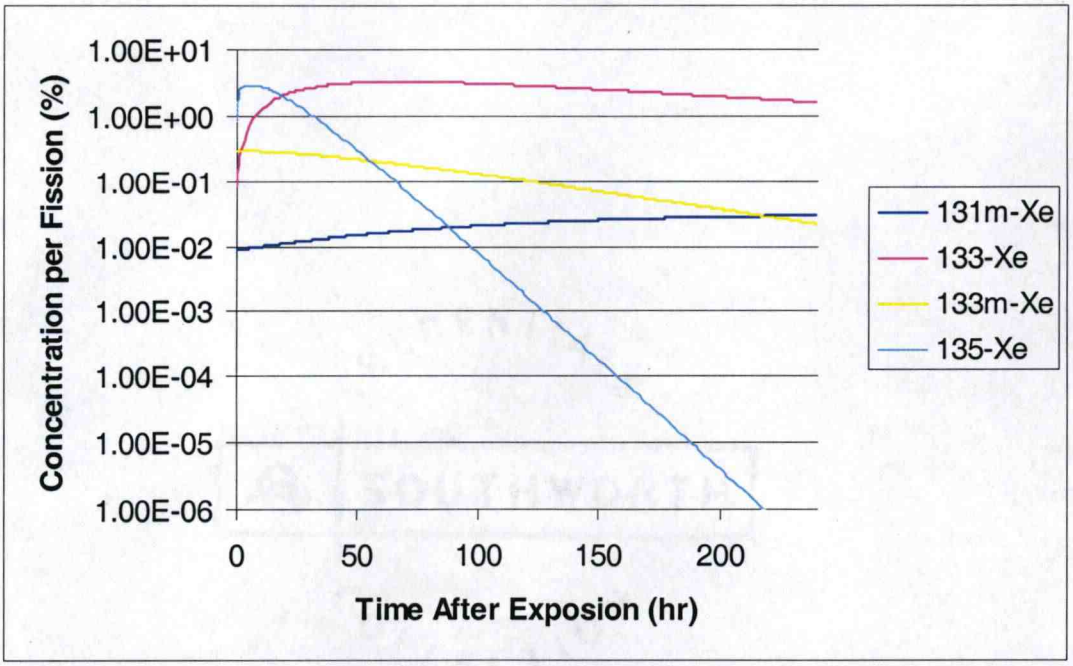

Figure 4.3 Expected radioxenon concentrations (%) following high-energy fission of ^{239}Pu.

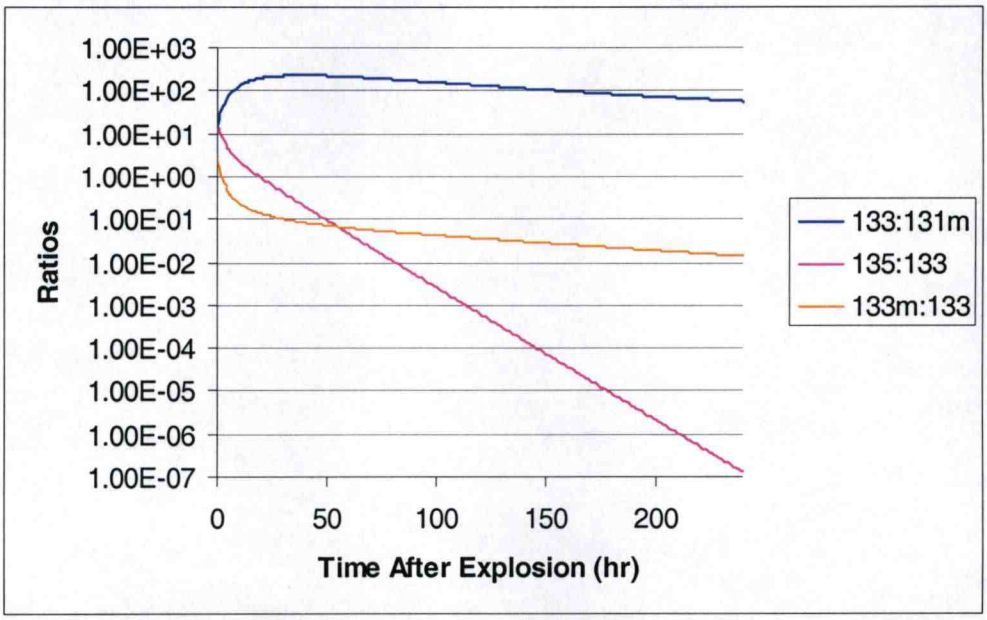

Figure 4.4 Expected radioxenon concentration ratios following high-energy fission of ^{239}Pu.

The concentration ratios in Figures 4.2 and 4.4 were generated by this author using ENDF data with decay chains modeled in STELLA. Ratios determined herein are similar to those generated by Heimbigner et al (2002) (see Figure 2.3). As time after detonation increases, and the ratios of ^{131}Xe:^{133}Xe, ^{133m}Xe:^{133}Xe, and ^{135}Xe:^{133}Xe are changing, the resultant spectra will change accordingly. Similarities and differences among radioxenon concentrations following ^{235}U and ^{239}Pu fission will be discussed in Section 4.2.1.

By knowing the number of fissions in a "typical" nuclear weapons test (as described in Section 2.2.1) and the radioxenon concentrations presented in Figures 4.1 and 4.3, the total amount of activity of the four nuclides was determined. Activity is shown in Curies in Table 4.1.

Table 4.1 Total radioxenon activity following a "typical" nuclear weapon detonation.

Time After Fission (hr)	Activity (Ci) from ^{235}U	Activity (Ci) from ^{239}Pu
0	6.1E+08	2.3E+09
24	5.5E+09	7.6E+09
48	5.2E+09	6.8E+09

4.2 Photon Simulations

The following are the results of simulations of photon interactions in the phoswich detector performed in MCNP5 as described in Chapter 3. All simulations contained 20,000,000 photon histories. Figures 4.5- 4.7 are resultant radioxenon spectra from high energy fission of ^{235}U beginning with the spectrum at t=0 hr, followed by t= 24hr, and t=48 hr after fission. Likewise, Figures 4.8- 4.10 present resultant spectra from high energy fission of ^{239}Pu at identical time increments.

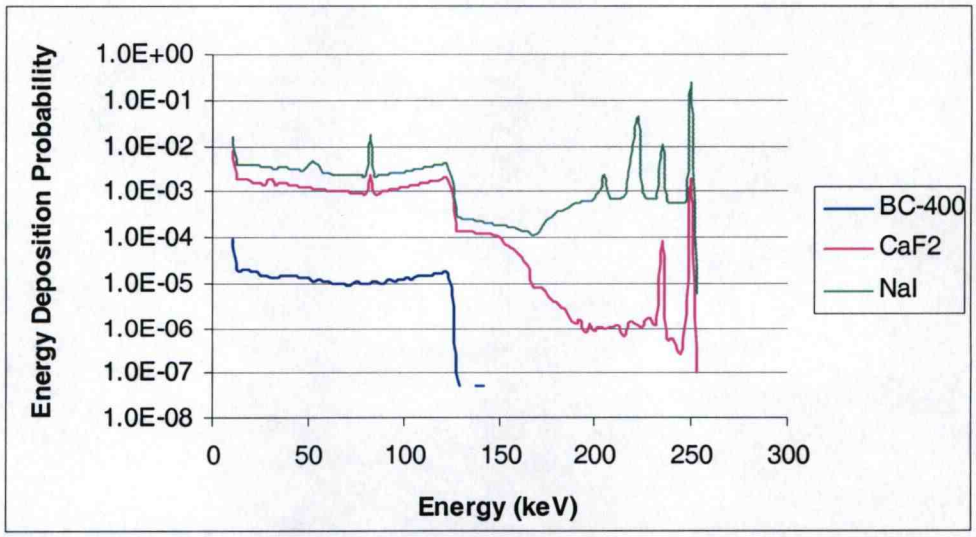

Figure 4.5 Radioxenon spectra from high-energy fission of ^{235}U in all three scintillation crystals with radioxenon ratios at t=0 after fission.

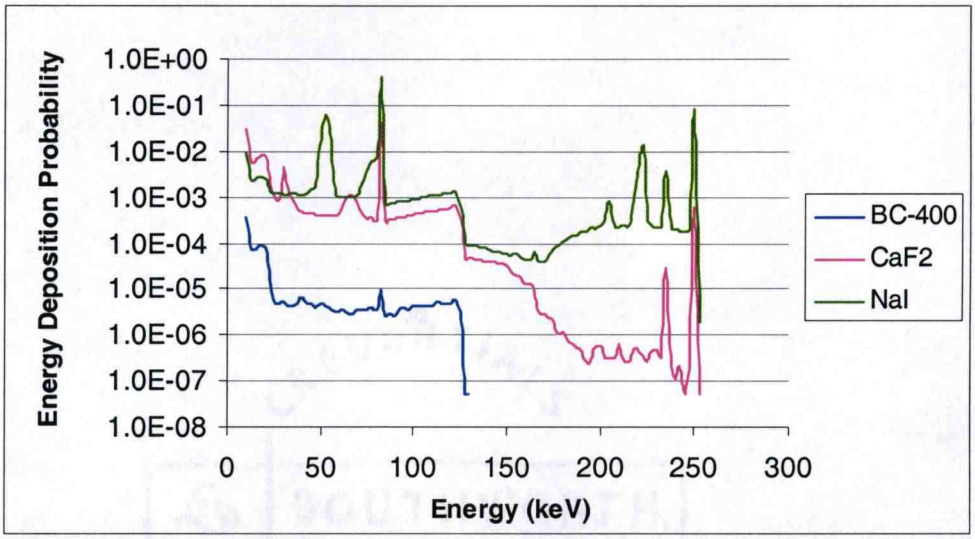

Figure 4.6 Radioxenon spectra from high-energy fission of ^{235}U in all three scintillation crystals with radioxenon ratios at t=24h after fission.

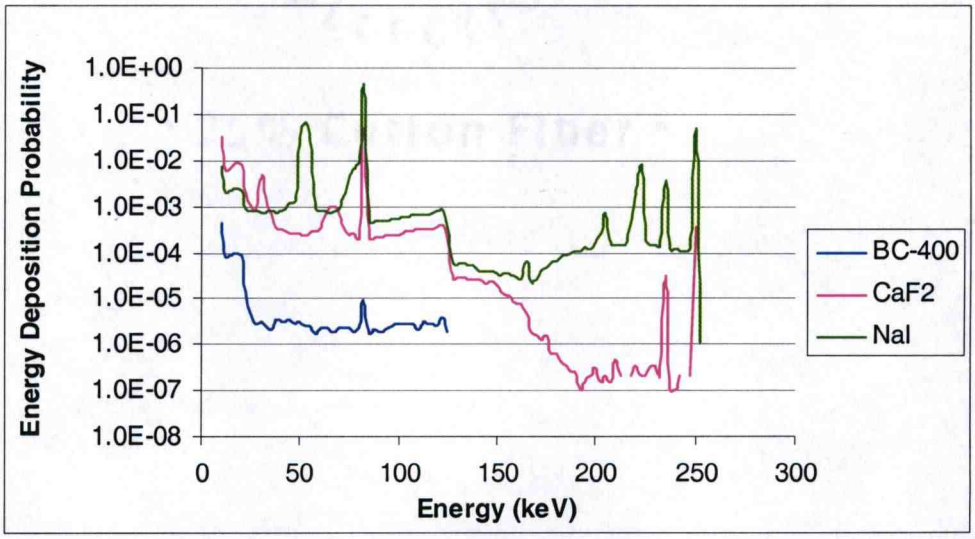

Figure 4.7 Radioxenon spectra from high-energy fission of ^{235}U in all three scintillation crystals with radioxenon ratios at t=48h after fission.

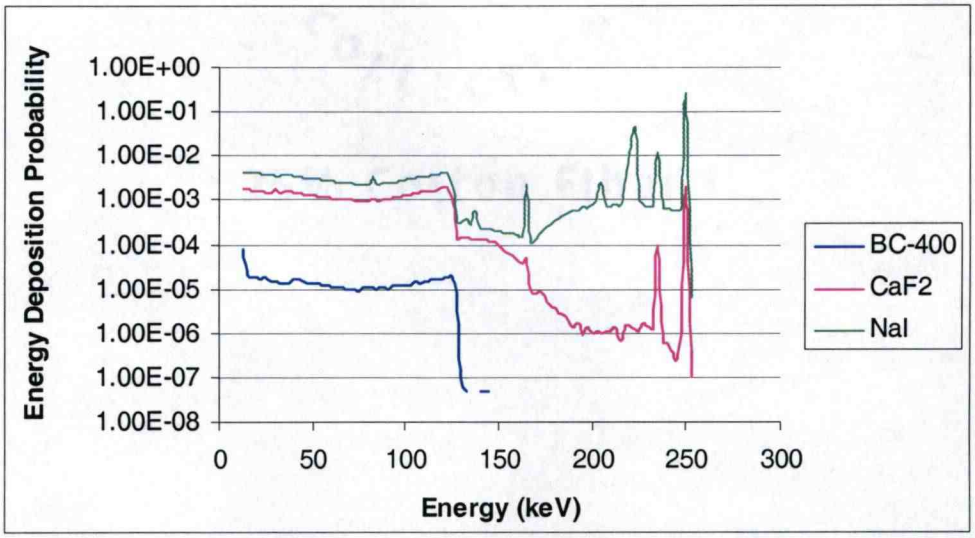

Figure 4.8 Radioxenon spectra from high-energy fission of ^{239}Pu in all three scintillation crystals with radioxenon ratios at t=0 after fission.

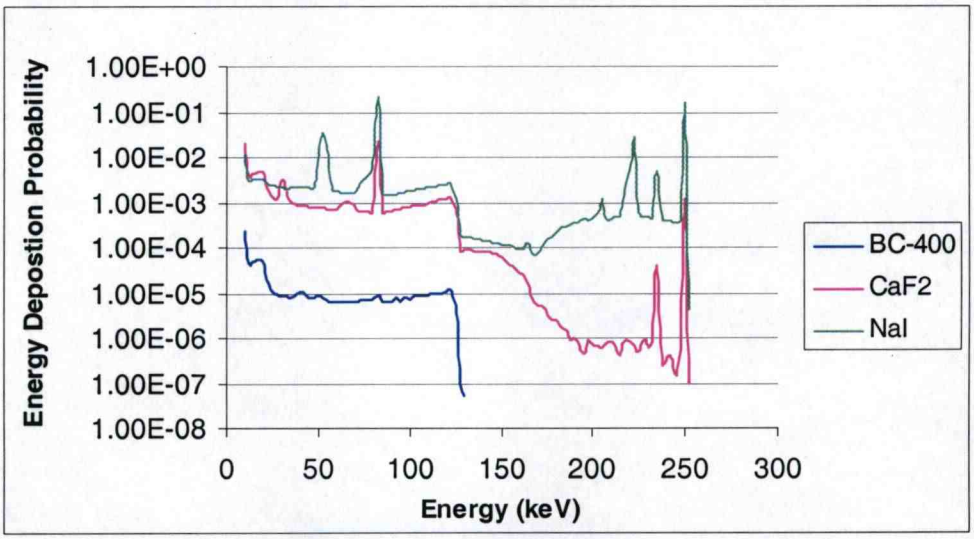

Figure 4.9 Radioxenon spectra from high-energy fission of ^{239}Pu in all three scintillation crystals with radioxenon ratios at t=24h after fission.

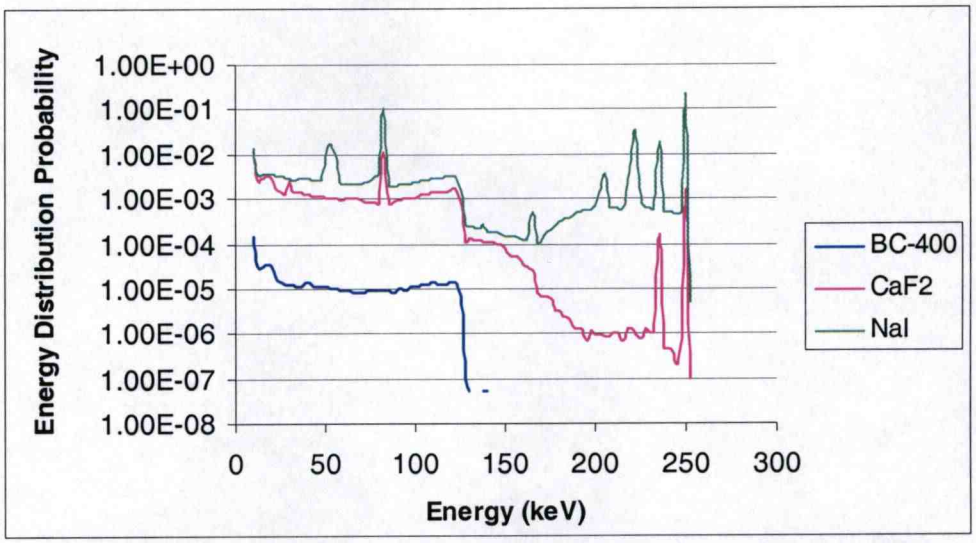

Figure 4.10 Radioxenon spectra from high-energy fission of ^{239}Pu in all three scintillation crystals with radioxenon ratios at t=48h after fission.

In all spectra, the Compton continuum is present with a very discernable Compton edge in all scintillation materials. The edge occurs as a result of interactions of the 250 keV photon emitted during the decay of ^{135}Xe. During Compton scatter, the photon can be scattered through all angles, with a scatter of 180° transferring the maximum amount of energy to the recoil electron. The Compton edge occurs at the energy corresponding to the maximum recoil electron energy. The location of the edge is determined using the following equation taken from Knoll (2000);

$$E_{e^-} = h\nu\left(\frac{\left(h\nu / m_o c^2\right)\left(1-\cos\theta\right)}{1+\left(h\nu / m_o c^2\right)\left(1-\cos\theta\right)}\right) \qquad (1)$$

where hν is the energy of the incoming photon, m_oc^2 is the rest mass energy of the electron (511 keV), and θ is the angle of the scattered photon. The location of the Compton edge, therefore, is at 123.6 keV.

The BC-400 spectra results almost entirely from Compton events with virtually no discernable photopeaks. Recall that BC-400 is an organic scintillator composed

purely of hydrogen and carbon. Because of the low Z of the material, there is effectively no photoelectric cross section for the simulated gamma energies emitted.

The four full-energy peaks of interest (equal to initial gamma energies of photons from the radioxenon isotopes), should and do occur in NaI(Tl) at 80.9, 163.9, 233.2, and 250.0 keV, respectively. It is evident from Figures 4.5- 4.10, however, that additional peaks are also prominent in the NaI(Tl) component of the spectra. During the photoelectric absorption process, an incoming photon interacts with a bound inner-shell electron and ejects it from the atom, creating a vacancy in the electron shells. The energy of the ejected electron is equal to that of the incoming photon minus the binding energy of the electron in its particular orbit. Because this vacancy must be filled to stabilize the atom, a characteristic x-ray is emitted by the absorber atom as the orbital electrons rearrange. In this case, sodium is the absorber atom, emitting a maximum characteristic x-ray of 30.6 keV (http://physics.nist.gov 2006). The energy deposited by the resultant ejected electron is 30.6 keV less than the full-energy peak, producing additional peaks at 50.4, 133.3, 202.6, and 219.4 keV, respectively. Typically, the kinetic energy of the ejected electron and the x-ray are both fully absorbed in the medium of the detector and simultaneously detected as one signal[9]. Inherent in the F8 tally of MCNP5, the simulation is strictly recording each individual energy deposition, therefore separately recording the deposition of the ejected electron, producing the four additional peaks.

[9] The NaI(Tl) scintillator on the triple-layer phoswich at OSU does not have the resolution needed to detect the x-ray energy deposition separate from the ejected electron energy deposition.

Under actual operating conditions of the phoswich detector, these peaks will be much less prominent than the F8 tally demonstrates. The reason this peak may exist at all during actual radioxenon detection is due to one particular case where a photoelectric event occurs near a surface of the detector. In this instance, the x-ray photon may escape, and the energy deposited by the ejected electron will be equal to the energy of the photopeak minus the characteristic x-ray energy. These peaks are known as x-ray escape peaks, termed accordingly as the x-ray "escapes" the volume of the detector. These escape peaks are hereafter excluded from the discussion.

All simulated photon spectra from high-energy fission of ^{235}U and ^{239}Pu demonstrate expected results for the three scintillation materials. BC-400 had the fewest number of interactions (because of the very thin width and low Z), followed by $CaF_2(Eu)$ (again with relatively thin width and low Z), with the majority of energy deposition occurring in the NaI(Tl) scintillation crystal (due to sufficient thickness and high Z).

4.2.1 Time After Fission

As evident from Figures 4.2 and 4.4, isotopic ratios are changing with time; therefore, the resultant spectra will change with time. Figures 4.11 (radioxenon fission spectra from ^{235}U) and 4.12 (radioxenon fission spectra from ^{239}Pu) demonstrate the differences in the NaI(Tl) spectra as time after detonation increases.

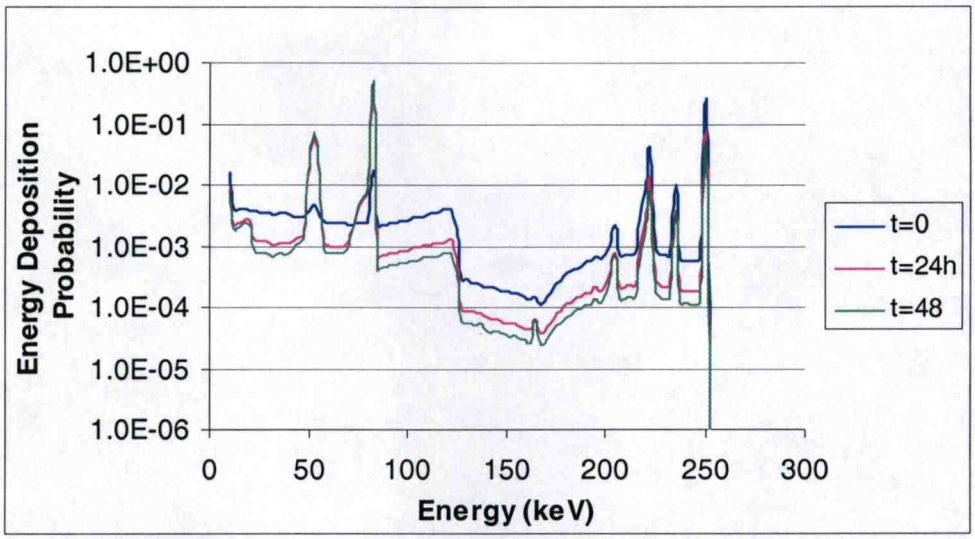

Figure 4.11 Radioxenon spectra from high-energy fission of ^{235}U in NaI(Tl) scintillator at t=0, t=24h, and t=48h after fission.

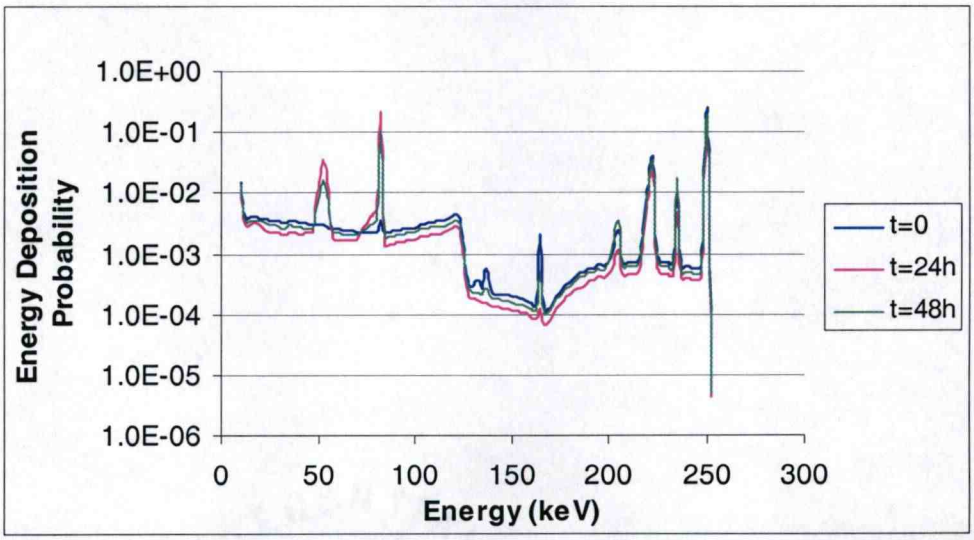

Figure 4.12 Radioxenon spectra from high-energy fission of ^{239}Pu in NaI(Tl) scintillator at t=0, t=24h, and t=48h after fission.

In both figures, the 80 keV peak (produced during the decay of ^{133}Xe), becomes increasingly prominent with time as the ^{133}Xe concentration increases. There is a small increase in the 163 keV peak (produced during the decay of ^{131m}Xe) in Figure 4.11, as the amount of ^{131m}Xe is slowly increasing. The same peak on the ^{239}Pu

fission spectra becomes less prominent as time increases, as the concentration of ^{131m}Xe is very small relative to the other three radioxenons (see Figure 4.3).

4.3 Beta Simulation

The results of a ^{133}Xe beta spectrum simulated with 10,000,000 source particles appear in Figure 4.13.

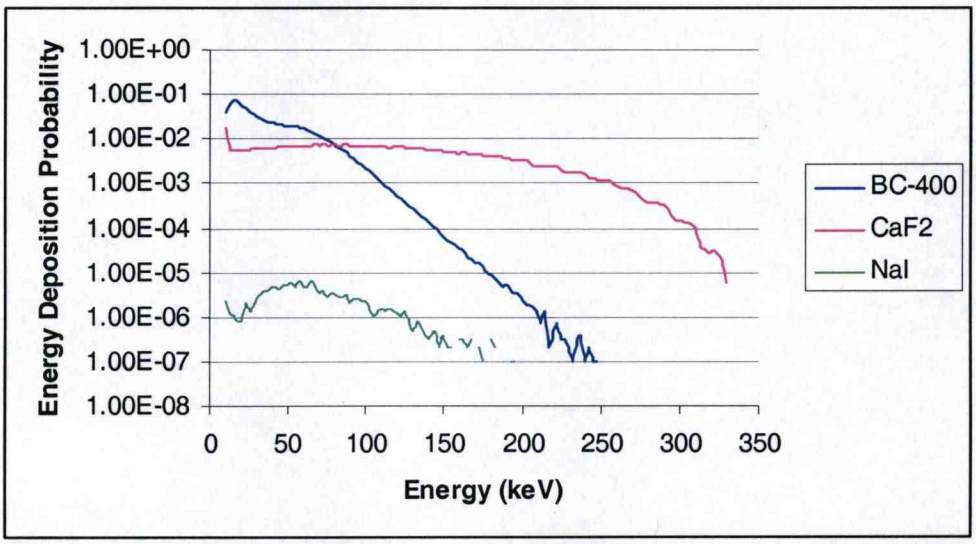

Figure 4.13 Beta Energy Spectra for ^{133}Xe in BC-400, CaF_2 and NaI with 1,000,000 simulated particles.

A significant number of beta particle interactions (<3% error) occurred with the BC-400 scintillation material yielding energy depositions up to 140 keV, with a very small number of depositions beyond and to 258 keV. A significant number of beta particle interactions (<3% error) occurred with the $CaF_2(Eu)$ scintillator yielding energy depositions up to 310 keV, with a small number of depositions occurring beyond and to 330 keV.

As both the BC-400 and $CaF_2(Eu)$ scintillation crystals are sufficient for beta detection, very little energy deposition occurred in the NaI(Tl). The NaI(Tl)

component shown in Figure 4.13 is not a continuous line, as there was not a sufficient number of energy depositions to produce a continuous spectrum. No energy bins recorded errors less than 13%. According to calculations described in Chapter 3, the energy of an electron must be greater than about 1.4 MeV to pass through the BC-400 and CaF_2(Eu) layers, and if quartz is included, the electron needs about 2.6 MeV to pass through all three layers. As is evident in Figure 4.13, a beta simulation run with a maximum beta energy of 346.5 keV did produce a small amount of energy deposition in NaI(Tl). The energy deposition events in NaI(Tl), however, are most likely attributed to Bremsstrahlung photon radiation produced in either BC-400 or CaF_2(Eu). As demonstrated by photon simulations, low energy photons can pass through the layer of BC-400, CaF_2(Eu), and quartz with minimal interaction, ultimately exiting the phoswich system or depositing energy in NaI(Tl).

4.4 Detector Response Determination

The data presented in the previous sections provides information regarding the probabilities of energy deposition. However, the analysis must be taken further to determine the detector response to individual energy deposition events, i.e. fundamental signal shape. The basic sequence of events for detection in the phoswich system is as follows:

Interaction→ Energy Deposition→ Light Conversion→ Photoelectron Production→ Electron Multiplication→ Signal from PMT

In order to construct a simulated signal, the energy deposited in each layer must be determined for a given photon interaction history. MCNP5, with the addition of the

PTRAC card, was used to simulate energy deposition and further to simulate representative pulse shapes for specific energy-deposition events. The output file created by PTRAC provides a large amount of information (See Section 3.4.1 PTRAC) that must be analyzed to understand the photon and particle interaction history. The simulation was executed with 1,000,000 events, which corresponded to 297,672 photons, i.e. on average each photon experienced about three interactions. From these individual photon histories, the amount of energy deposited, and the layer in which the deposition occurred can be extracted. In Table 4.2, the seven interaction scenarios are listed along with their probability of occurrence.

Table 4.2 Seven scenarios for light output signals with resultant MCNP simulation data.

Scenario	BC-400	$CaF_2(Eu)$	NaI(Tl)	Probability
1	X			6.0E-04
2		X		0.081
3			X	0.57
4	X	X		7.0E-05
5	X		X	1.0E-04
6		X	X	0.017
7	X	X	X	7.0E-06

Of these resultant occurrences, 32 particle histories (the first five histories of each scenario, with two from scenario #7) were examined in detail to determine (1) the amount of energy deposited in each scintillation layer, and (2) the resultant signal pulse expected for that energy deposition pattern. Table 4.3 displays data obtained from these 32 histories.

Table 4.3 Energy deposition for photon simulations in each layer for all possible scenarios.

		BC-400	CaF_2	NaI
Scenario	Initial E (keV)	E Deposited (keV)	E Deposited (keV)	E Deposited (keV)
1	250	103.88		
	250	91.46		
	250	13.05		
	250	14.66		
	81	17.55		
2	81		18.70	
	250		0.68	
	164		5.08	
	81		81.00	
	250		19.00	
3	81			81.00
	81			52.70
	250			250.00
	81			52.40
	250			250.00
4	81	0.40	18.30	
	250	38.33	87.17	
	81	68.10	3.60	
	250	17.84	232.16	
	81	0.63	0.69	
5	250	0.04		41.07
	250	60.32		189.68
	81	2.87		78.13
	233	30.61		202.39
	233	17.50		215.50
6	81		2.70	52.70
	81		0.60	80.40
	250		78.05	28.61
	233		32.67	200.33
	250		34.01	92.89
7	250	80.42	40.57	129.01
	81	3.23	0.80	76.97

By knowing the energy deposition per layer, we can construct the relative signal output (shape) expected from the PMT. The total relative signal output, F(t), is equal to the sum of contributions from each layer, such that:

$$F(t) = Ae^{-\frac{t}{\tau_1}} + Be^{-\frac{t}{\tau_2}} + Ce^{-\frac{t}{\tau_3}}, \quad (2)$$

where A is the relative signal strength for BC-400, B for $CaF_2(Eu)$, and C for NaI(Tl), and τ_1, τ_2, and τ_3 are the primary decay times for each scintillator respectively. The integral of the contribution from each layer is proportional to the energy deposited in that layer. The integral, therefore, of F(t) is proportional to the total energy deposited in all layers where,

$$\int F(t)dt = \int Ae^{-\frac{t}{\tau_1}}dt + \int Be^{-\frac{t}{\tau_2}}dt + \int Ce^{-\frac{t}{\tau_3}}dt, \quad (3)$$

which is equal to,

$$\int F(t)dt = \tau_1 A(1-e^{\frac{-t}{\tau_1}}) + \tau_2 B(1-e^{\frac{-t}{\tau_2}}) + \tau_3 C(1-e^{\frac{-t}{\tau_3}}), \quad (4)$$

when evaluated from zero to t. In order to determine values for the coefficients A, B, and C (relative signal strength of energy deposition in each scintillator), the relative contribution from each layer is set equal to the individual integral of that particular scintillation layer. This is shown below for BC-400;

$$F_A(t) = \tau_1 A(1-e^{\frac{-t}{\tau_1}}), \quad (5)$$

where $F_A(t)$ is the relative contribution from BC-400, $F_A(t) = E_A \bullet R_A$, and E_A is energy deposited and R_A is the relative light output in scintillator A (see Table 3.2). Once A, and similarly B and C, are determined, their values are used in Equation (2) to generate the resultant signal pulse shape F(t).

For example, referring to the first occurrence of scenario #7 found in Table 4.2, an energy deposition of 80.42 keV was simulated to have occurred in BC-400, 40.57 keV in CaF_2(Eu), and 129.01 keV in NaI(Tl). The product of these values and the relative light output for each scintillator yields 20.91 for BC-400, 20.285 for CaF_2(Eu) and 129.01 for NaI(Tl); these values are then set equal to the integral of the light output from the respective layer. Evaluating Equation (5) for t→ 1000 ns, the value of A is solved as follows:

$$20.91 = (2.4ns * A)(1 - e^{\frac{-1000ns}{2.4ns}}),$$

$$\text{and } A = 8.7125.$$

Similarly, B and C are determined to be 0.03295 and 0.52567, respectively. The values of the coefficients are then used in Equation (2) and the resultant signal pulse is predicted (Figure 4.14).

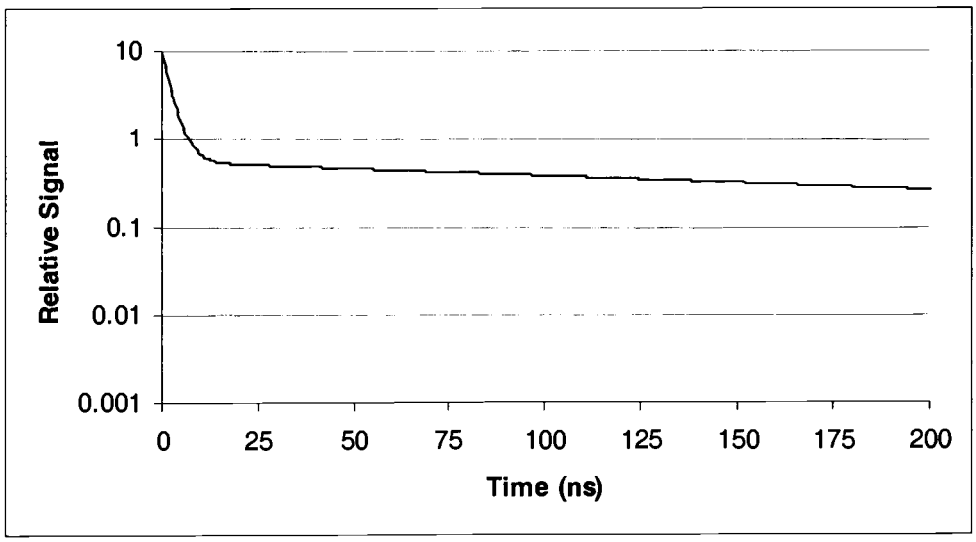

Figure 4.14 Relative signal from energy deposition of 80.42 keV in BC-400, 40.57 keV in CaF_2(Eu), and 129.01keV in NaI(Tl).

Two more examples are presented in Figure 4.15 to illustrate the difference in signal output for an occurrence in scenario #4 (deposition in BC-400 and $CaF_2(Eu)$) and an occurrence of scenario #5 (deposition in BC-400 and NaI).

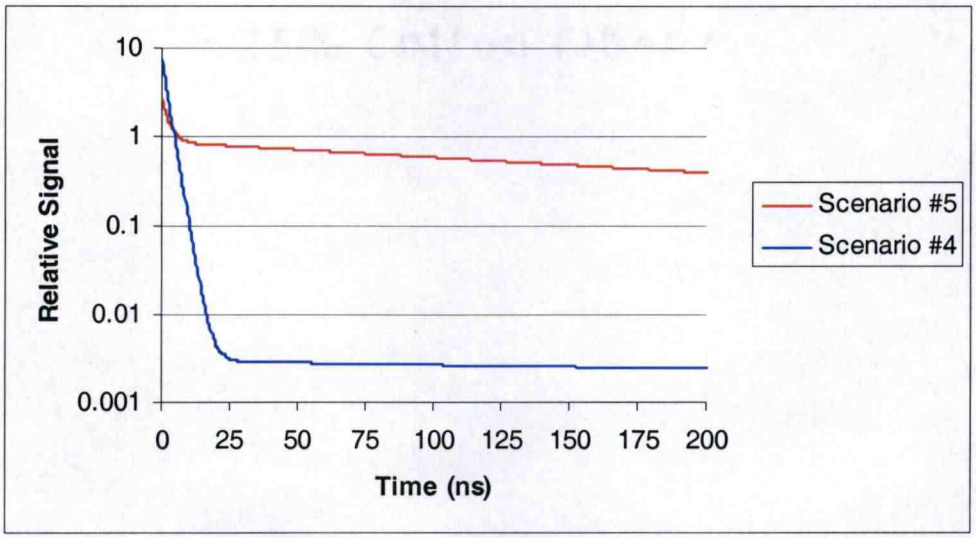

Figure 4.15 Relative signal from 3rd occurrence of scenario #4, and relative signal from 5th occurrence of scenario #5 (see Table 4.2 for energy deposition).

Notice that the "Scenario #4" signal decays much faster than "Scenario #5" signal. "Scenario #4" was created from a simulated energy deposition of 68.10 keV in BC-400 and 3.60 keV in CaF2(Eu). Because almost all the energy was deposited in BC-400 (2.4 ns decay time), the signal will decay much faster than "Scenario #5" which contained a significant amount of energy deposition (215.50 keV) in NaI(Tl) (decay time of 250 ns). Also, notice the relative signal of "Scenario #5" (caused by an energy deposition of only 17.50 keV in BC-400) begins with a smaller initial value than "Scenario #4" and the signal in Figure 4.14.

4.4.1 Evaluation of Relative Signal Pulse

The signal pulses from all 32 events listed in Table 4.3 were calculated in the same manner and analyzed by a component analysis (CA) algorithm, developed at OSU, that operates in reverse to the procedures described in Section 4.4. The purpose of the algorithm is to achieve clear separation between the three decay components (BC-400, CaF_2(Eu), NaI(Tl)) of each signal pulse to back-calculate the amount of energy deposited in each scintillation crystal, given a specific signal pulse as input. This process of deducing the individual contributions to a recorded signal pulse is similar to spectral deconvolution. Due to the fact that there exist inherent uncertainties in detector response and statistical variance in the measured energies, only estimations can be made of the incident energy.

The algorithm begins at the apex of the pulse (t=0) and operates using a least squares fit method to assign the most accurate values to each of the three components of the pulse. This is accomplished by first simplifying Equation (2) to

$$F[n] = Af_a[n] + Bf_b[n] + Cf_c[n], \tag{6}$$

where F[n] is the actual signal output, $f_a[n]$ is the response of the system to BC-400, $f_b[n]$ to CaF_2(Eu), and $f_c[n]$ to NaI(Tl), and are all known functions. The coefficients A, B, and C are relative contributions from each layer, and are unknown. Each signal can be fit with a least squares method as follows:

$$M = \sum_{n=0,N} (S[n] - F[n])^2 \tag{7}$$

where S[n] is the estimated signal, and N is the number of sample points. A least squares fit is a mathematical technique used to find the best fit curve to a given set of points by minimizing the sum of the squares of the residuals (Equation (7)). Each incoming signal is evaluated using this method, and the values of A, B, and C are returned, in order to estimate the amount of energy deposited in each scintillator. Accuracy of the algorithm had yet to be evaluated.

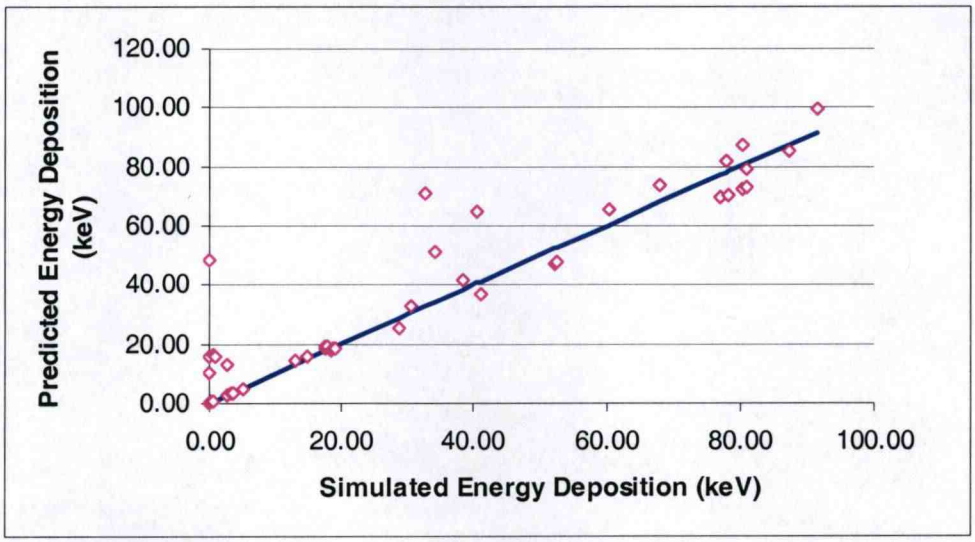

Figure 4.16 Simulated energy deposition vs. predicted energy deposition in all layers of the phoswich detector.

Figure 4.16 is a plot showing simulated versus predicted energy deposition in different layers of the phoswich. The solid line represents a slope of 1 where the predicted and the simulated energies are identical. The open diamonds (60 data points) represent the prediction of energy deposition based on the CA algorithm. It can be seen from Figure 4.16 that the algorithm produces reasonable results with the exception of three outliers around the simulated deposition of ~40 keV and several outliers at very low energy deposition. The three outliers around 40 keV were

overestimations by the algorithm of the amount of energy deposited in the CaF_2(Eu) layer. The majority of the outliers around 0 keV were produced during the evaluation of occurrences as scenario #3 (deposits in NaI(Tl) only) and scenario #5 (deposits in BC-400 and NaI(Tl). The CA algorithm falsely predicted energy deposition in the CaF_2(Eu) layer where MCNP simulations yielded no deposits. Modifications to the algorithm may be required to minimize error, as eventually the algorithm will be integrated into the phoswich system to achieve real-time signal component analysis.

Chapter 5 CONCLUSIONS AND FUTURE WORK

In this study, fission mechanisms were reviewed in detail by examining Q-values, energy balance, and fission product yield. Typical nuclear weapons detonations (fissile materials of ^{235}U and ^{239}Pu) were studied and radioxenon ratios (^{131m}Xe:^{133}Xe, ^{133m}Xe:^{133}Xe, and ^{135}Xe:^{133}Xe) were determined. These ratios will be required to discriminate between reactor related radioxenon and those expected from possible underground nuclear detonations.

MCNP5 was used to model a prototype phoswich detector to establish important detector response characteristics to photons and electrons. Radioxenon decay rates and energies were inputted into the source card of the model allowing the study of energy deposition characteristics in each scintillation layer of the phoswich detector. The detector yielded simulated photon energy spectra producing expected full-energy peaks.

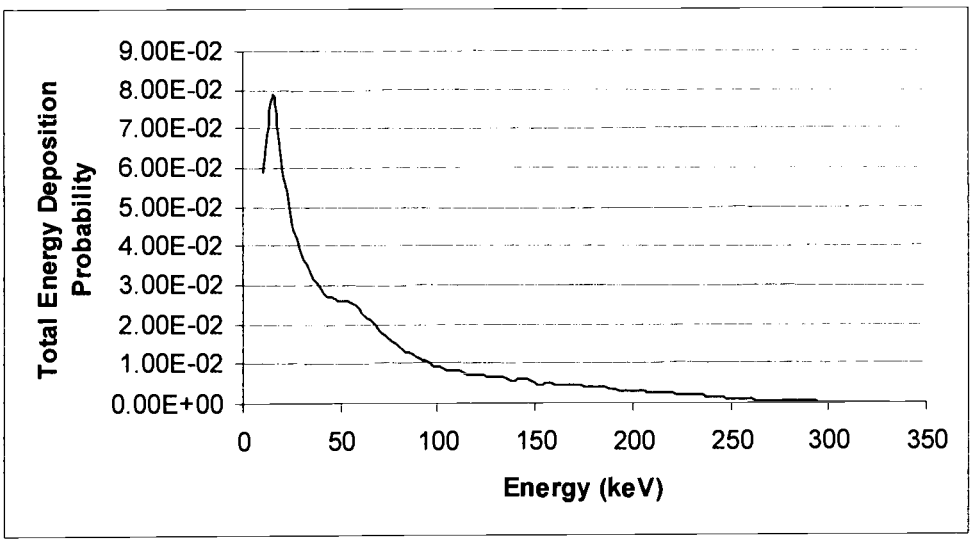

Figure 5.1 Beta energy spectra for ^{133}Xe totaled from all three scintillation materials.

Beta simulations demonstrate excellent detector response, particularly in the BC-400 and $CaF_2(Eu)$ layers as shown in Figure 5.1. The spectra resembles the beta emission spectra of ^{133}Xe (Figure 3.6).

Detector response was determined from several energy deposition scenarios created by decay energies specific to radioxenons. The PTRAC card is a useful tool to determine energy deposition and location of energy deposition in order to construct simulated pulse shapes. Simulated output pulses were then evaluated by a CA algorithm developed at OSU to predict the quantity of energy deposited in each scintillation layer. The algorithm had yet to be tested, and achieved clear separation of energy deposition in each scintillator in most cases. This is very important as the algorithm will eventually be incorporated into the Phoswich detection system. Minimal modifications to the algorithm will be required, however, to eliminate false predictions of energy deposition in the $CaF_2(Eu)$ layer, as false predictions will cause rejections of otherwise valid pulses.

This work will guide future detector development, including optimization of the phoswich design, specifically by varying the width of the scintillation crystals to obtain a more efficient and effective measurement system. Construction of the optimized phoswich detector will then be followed with a new focus on determining true detector response in a laboratory setting. This will necessitate the preparation of a beta source with minimal self-absorption and minimal backscatter.

Research performed herein will also assist in pulse shape discrimination characteristics and development of a digital pulse processing system. In order to

determine a comprehensive analysis of detector response, future work should consider running a similar PTRAC analysis on ^{133}Xe and ^{135}Xe beta decay simulations, as well as the response to conversion electrons resulting from the decay of all four radioxenons. Current supporting research at OSU is heavily focused on the development of a high-speed digital signal analysis technique that will allow for real-time measurement of radioxenons.

References

1. Bush-Goddard, S.P., Beta Spectroscopy Using Deconvolution and Spectral Stripping Techniques with a Triple Layer Phoswich Detector, University of Michigan, Ann Arbor, MI: Doctoral Dissertation, April 2000.

2. Kriss, A.; Hamby, D.M. Scintillation Beta Dosimetry and Spectroscopy Utilizing a Large Area Avalanche Photodiode. Proceedings of the Forty-eighth Annual Meeting of the Health Physics Society. San Diego, CA. *Health Physics*. 84(6): S168; 2003.

3. Kriss, A.A.; Hamby, D.M. Beta Spectroscopy with a Large-area Avalanche Photodiode Module and a Plastic Scintillator. *Nuclear Instruments and Methods in Physics Research - Section A*. 525(3): 553-559, June 2004a.

4. Kriss, A.A.; Hamby, D.M. Measurement and Modeling of Dose from External Beta Emitters Utilizing Plastic Scintillator Volumes. *Health Physics*. submitted March 2004b.

5. Kriss, A.A.; Hamby, D.M. Monte Carlo Based Enhancement of Beta Spectra by Removal of Fractional Energy Deposition Events in a Plastic Scintillator. *Nuclear Instruments and Methods in Physics Research – Section A.*. submitted April 2004c.

6. Tavakoli-Farsoni, A.; Hamby, D.M.; Bush-Goddard, S.P. A Performance Study on a Triple-layer Phoswich Detector for Beta Spectroscopy. Proceedings of the Forty-ninth Annual Meeting of the Health Physics Society. Washington, DC. *Health Physics*. 86(6): S144; 2004a.

7. Tavakoli-Farsoni, A.; Hamby, D.M. Optimization Modeling of Two Multi-layer Phoswich Detector Designs Using MCNP. *Health Physics*. submitted. Dec. 2004b.

8. US State Department. Available at: http://www.state.gov/www/global/arms/ctbtpage/trty_pg.html Accessed 2006.

9. Pacific Northwest National Laboratory. ARSA figure. Available at: www.pnl.gov Accessed 2006.

10. Ely, J.H.; Aalseth, C.E.; Hayes, J.C.; Heimbigner, T.R.; McIntyre, J.I.; Miley, H.S.; Panisko, M.E.; Ripplinger, M. Novel Beta-gamma Coincidence Measurements Using Phoswich Detectors. 25th Seismic Research Review. 533-541; 2003.

11. Martin James E. Physics for Radiation Protection. Weinheim: WILEY-VCH Verlag GmbH & Co. KGaA, 2004.

12. Glasstone S.; Dolan P.J. The Effects of Nuclear Weapons, 3rd Edition. U.S. Department of Defense, Energy Research and Development Administration. 1977.

13. Wikipedia. Fission of ^{233}U. Available at: www.wikipedia.org Accessed 2006.

14. Cember, H. Introduction to Health Physics Third Edition. New York: McGraw-Hill, 1996.

15. Lilley J. S. Nuclear Physics Principles and Applications. New York: John Wiley & Sons, Inc., 2004.

16. Robbins D.J.; Rynes J.; Biegalski K.F. Radionuclide Software Installation at the US National Data Center. 24th Seismic Research Review 711-720, 2002.

17. Heimbigner, T.R.; McIntyre, J.I.; Bowyer, T.W.; Hayes, J.C.; Panisko, M.E. Environmental Monitoring of Radioxenon in Support of the Radionuclide Measurement System of the International Monitoring System. 24th Seismic Research Review. 694-700, 2002.

18. Knoll, G.F. Radiation Detection and Measurement. 3rd Edition. John Wiley and Sons, Inc. New York, 2000.

19. Grindlay J.E.; Prince T.A.; Gehrels N.; Tueller J.; Hailey C.J.; Ramsey B.D.; Weisskopf M.C.; Ubertini P.; Skinner G.K. Energetic X-ray Imaging Survey Telescope (EXIST). Available at www.nasa.gov. 1994.

20. Pak R.; Bjarki O.; Hannuschke S.A.; Lacey R.A.; Lauret J.; Llope W.J.; Nadasen A.; Stone S.T.B.; Vander Molen A.M.; Westfall G.D. Momentum Dependence of the Nuclear Mean Field from Peripheral Heavy-ion Collisions. The American Physical Society. 1996.

21. Hennig W.; Tan H.; Warburton W.K.; McIntyre J.I. Digital Pulse Shape Analysis with Phoswich Detectors to Simplify Coincidence Measurements of Radioactive Xenon. 27th Seismic Research Review. 787-794, 2004.

22. STELLA. What is STELLA. Available at: www.iseesystems.com Accessed 2006.

23. Evaluated Nuclear Data File. ENDF-349 Fission Product Yield. Available at: http://t2.lanl.gov

24. BICRON. What is BICRON. Available at: www.bicron.com Accessed 2006.

25. BICRON. CaF2(Eu) Scintillation Material Data Sheet. 2002.

26. BICRON. NaI(Tl) Properties of NaI(Tl). 1997.

27. BICRON. Technical Data of Bicron Plastic Scintillators. Available at: www.bicron.com Accessed 2006.

28. Childress N.L.; Miller W.H. MCNP Analysis and optimization of a Triple Crystal Phoswich Detector. Nuclear Instruments and Methods in Physics Research. 263-270. 2002.

29. National Nuclear Data Center. Radionuclide Decay Schemes. Available at: www.nndc.com Accessed 2006.

30. Eckerman K.F.; Westfall R. J.; Ryman J. C.; Cristy M. Availability of Nuclear Decay Data in Electronic Form, Including Beta Spectra not Previously Published. Health Physics 67(4):338-345. 1994.

Appendix A

Table A.1 ENDF Fraction of radionuclides produced from high-energy fission of ^{235}U and ^{239}Pu.

	^{235}U	^{239}Pu
Nuclide	Fission Yield (%)	Fission Yield (%)
Cd-131	1.38E-05	4.85E-06
In-131	0.007163	0.002742
Sn-131	0.368568	0.184435
Sb-131	2.150054	1.633232
Te-131m	1.164511	1.748264
Te-131	0.29159	0.383765
I-131	0.120171	0.402474
Xe-131m	0.000909	0.008882
Xe-131	0.000199	0.00195
In-133	5.21E-05	1.93E-05
Sn-133	0.019	0.007414
Sb-133	0.69893	0.343155
Te-133m	2.444996	1.752873
Te-133	0.536703	0.384775
I-133	1.656838	1.989637
Xe-133m	0.141766	0.294783
Xe-133	0.030148	0.087153
Cs-133	0.000833	0.005739
Sn-135	0.000169	7.81E-05
Sb-135	0.041463	0.021214
Te-135	1.044298	0.706595
I-135	3.1345361	3.229334
Xe-135m	0.996066	1.358887
Xe-135	0.4540701	0.865993
Cs-135	0.060539	0.192458
Ba-135	0.000298	0.002543